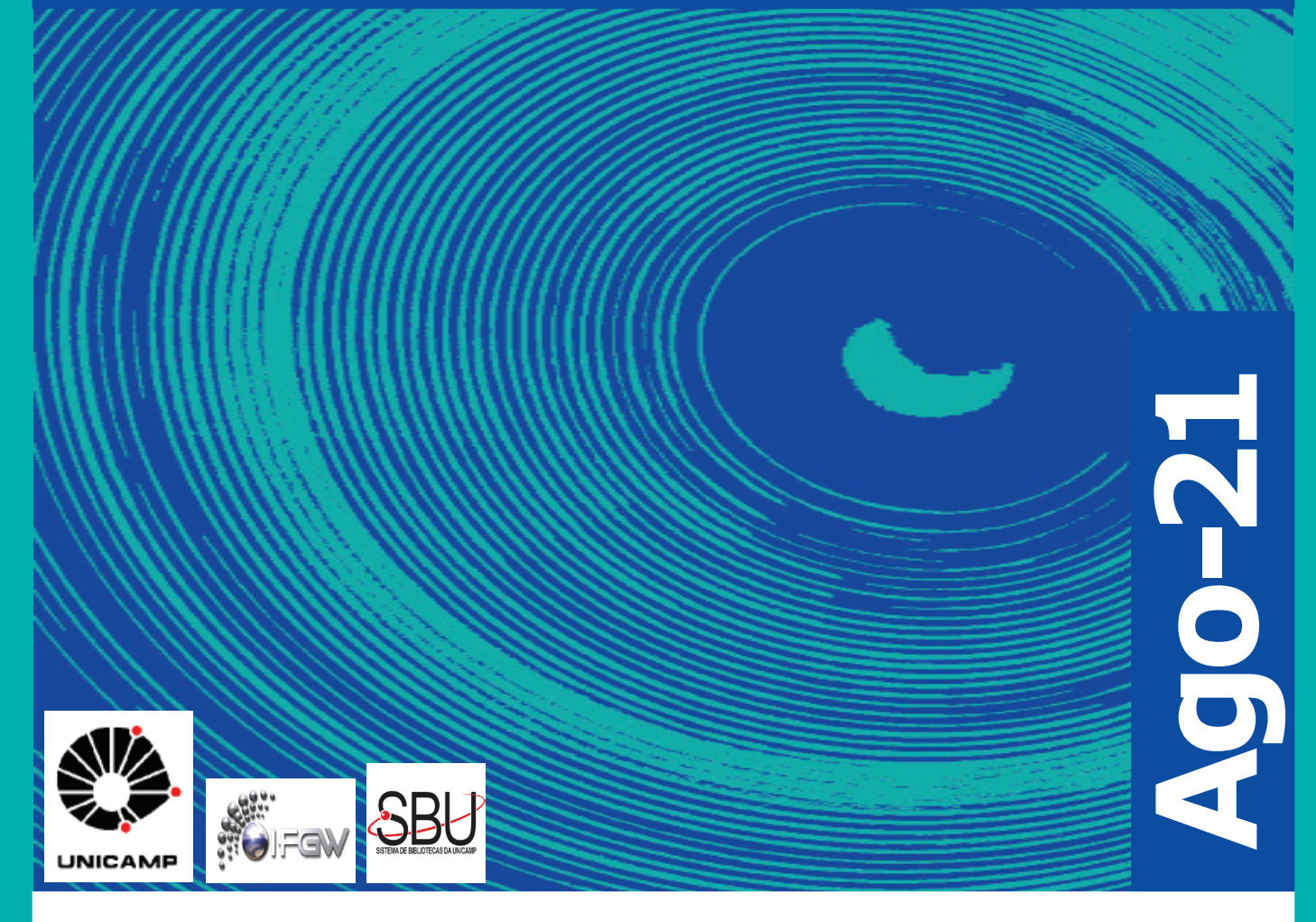
Abstracta

Ano XXV - N. 04



Artigos publicados P123-2021 à P199-2021

Materiais Editoriais Ma002-2021 à Ma003-2021

Patentes Pa001-2021 à Pa005-2021

Defesas de Dissertações do IFGW D012-2021 à D015-2021

Defesas de Teses do IFGW T008-2021 à T011-2021

Artigos publicados

[P123-2021] "Accurate modeling and characterization of photothermal forces in optomechanics"

Primo, A. G.*; Kersul, C. M.*; Benevides, R.*; Carvalho, N. C.*; Menard, M.; Frateschi, N. C.*; Assis, P. L. de*; Wiederhecker, G. S.*; Alegre, T. M. P.*

Photothermal effects have been pointed out as prominent sources of forces in optomechanical systems, competing with the standard radiation pressure interactions. In this article, we derive a novel and accurate model for the prediction of photothermal forces and establish how some previous proposals can be complemented to yield precise results. As a proof-of-concept, we perform numerical and experimental tests on GaAs microdisk cavities and obtain striking agreement with our framework, revealing the importance of considering surface photothermal forces and the effects of multiple thermal modes in microphotonic devices.

APL PHOTONICS 6[8], 086101, 2021. DOI 10.1063/5.0055201

[P124-2021] "Adipose tissue radiodensity: A new prognostic biomarker in people with multiple myeloma"

Cunha, A. D. Jr. da; Silveira, M. N.; **Takahashi, M. E. S.***; Souza, E. M. de; Mosci, C.; Ramos, C. D.; Brambilla, S. R.; Pericole, F. V.; Prado, C. M.; Mendes, M. C. S.; Carvalheira, J. B. C.

Objectives: Standard prognostic markers based on individual characteristics of individuals with multiple myeloma (MM) remain scarce. Body-composition features have often been associated with survival outcomes in different cancers. However, the association of adipose tissue radiodensity with MM prognosis has not yet, to our knowledge, been explored. Methods: Computed tomography at the third lumbar vertebra was used for body-composition analysis, including adipose tissue radiodensity, in 91 people with MM. Additionally, fludeoxyglucose F 18 (F-18-FDG) positron emission tomography was used to assess adipose tissue F-18-FDG uptake. Proinflammatory cytokine and adipokine levels were measured. Results: Event-free survival and overall survival were both shorter in participants with high subcutaneous adipose tissue (SAT) radiodensity. Those in the highest SAT radiodensity tertile had an independently higher risk for both overall survival (hazard ratio, 4.55; 95% confidence interval, 1.26-16.44; P-trend = 0.036) and event--free survival (hazard ratio, 3.08; 95% confidence interval, 1.02-9.27; P-trend = 0.035). Importantly, higher SAT radiodensity was significantly correlated with increased F-18-FDG adipose tissue uptake and proinflammatory cytokine (tumor necrosis factor and interleukin-6) levels, and with decreased leptin levels. Conclusions: SAT radiodensity may serve as a biomarker to predict host-related metabolic and proinflammatory milieu, which ultimately correlates with MM prognosis.

NUTRITION 86, 111141, 2021. DOI: 10.1016/j.nut.2021.111141

 $\cite{P125-2021}$ "Analogue models for Schwarzschild and Reissner-Nordstrom spacetimes"

Oliveira, C. C. de*; Mosna, R. A.; Pitelli, J. P. M.; Richartz, M.

We present analogue models for the Schwarzschild and Reissner-Nordstrom (RN) spacetimes based on unidirectional hydrodynamic flows. We show that, with appropriate coordinate transformations, sound waves in a moving fluid propagate as scalar fields at the equatorial sections of Schwarzschild and RN black holes. The coordinate associated with the direction of the flow plays the role of the radial coordinate in standard Schwarzschild/RN coordinates,

while the transversal spatial coordinate is related to the angular coordinate on each equatorial slice. The magnitude of the flow velocity is related to the mass and charge of the analogue black hole. Physical quantities like pressure and density remain finite at the analogue horizon, thereby resulting in sound waves that are well defined almost everywhere, except possibly at the analogue black hole singularity.

PHYSICAL REVIEW D 104[2], 024036, 2021. DOI 10.1103/Phys-RevD.104.024036

[P126-2021] "Angular spectrum influence and entanglement characterization of Gaussian-path encoded photonic qudits"

Borges, G. F.; Baldijao, R. D.*; Matoso, A. A.; Padua, S.

Entangled quantum states play an important role in quantum information science and also in quantum mechanics fundamental investigations. Implementation and characterization of technigues allowing for easy preparation of entangled states are important steps in such fields. Here we generated entangled quantum states encoded in photons' transverse paths, obtained by pumping a nonlinear crystal with multiple transversal Gaussian beams. This approach allows us to generate entangled states of two qubits and two qutrits encoded in a Gaussian transversal path of twin photons. We make a theoretical analysis of this source, considering the influence of the pump angular spectrum on the generated states, further characterizing those by their purity and entanglement degree. Our experimental results reveal that the generated states present both high purity and entanglement, and the theoretical analysis elucidates how the pump beams profile can be used to manipulate such photonic states.

JOURNAL OF THE OPTICAL SOCIETY OF AMERICA B-OPTICAL PHYSICS 38[6], 1958-1965, 2021. DOI: 10.1364/JOSAB.419688

[P127-2021] "Band gap measurements of monolayer h-BN and insights into carbon-related point defects"

Roman, R. J. P.*; Costa, F. J. R. C.*; Zobelli, A.; Elias, C.; Valvin, P.; Cassabois, G.; Gil, B.; Summerfield, A.; Cheng, T. S.; Mellor, C. J.; Beton, P. H.; Novikov, S. V.; Zagonel, L. F.*

Being a flexible wide band gap semiconductor, hexagonal boron nitride (h-BN) has great potential for technological applications like efficient deep ultraviolet light sources, building block for two-dimensional heterostructures and room temperature single photon emitters in the ultraviolet and visible spectral range. To enable such applications, it is mandatory to reach a better understanding of the electronic and optical properties of h-BN and the impact of various structural defects. Despite the large efforts in the last years, aspects such as the electronic band gap value, the exciton binding energy and the effect of point defects remained elusive, particularly when considering a single monolayer. Here, we directly measured the density of states of a single monolayer of h-BN epitaxially grown on highly oriented pyrolytic graphite, by performing low temperature scanning tunneling microscopy (STM) and spectroscopy (STS). The observed h-BN electronic band gap on defect-free regions is (6.8 +/- 0.2) eV. Using optical spectroscopy to obtain the h-BN optical band gap, the exciton binding energy is determined as being of (0.7 + /- 0.2) eV. In addition, the locally excited cathodoluminescence and photoluminescence show complex spectra that are typically associated to intragap states related to carbon defects. Moreover, in some regions of the monolayer h-BN we identify, using STM, point defects which have intragap electronic levels around 2.0 eV below the Fermi level.

2D MATERIALS 8[4], 044001, 2021. DOI 10.1088/2053-1583/ac0d9c

[P128-2021] "Breast glandularity and mean glandular dose assessment using a deep learning framework: Virtual patients study"

Massera, R. T.*; Tomal, A.*

Purpose: Breast dosimetry in mammography is an important aspect of radioprotection since women are exposed periodically to ionizing radiation due to breast cancer screening programs. Mean glandular dose (MGD) is the standard quantity employed for the establishment of dose reference levels in retrospective population studies. However, MGD calculations requires breast glandularity estimation. This work proposes a deep learning framework for volume glandular fraction (VGF) estimations based on mammography images, which in turn are converted to glandularity values for MGD calculations. Methods: 208 virtual breast phantoms were generated and compressed computationally. The mammography images were obtained with Monte Carlo simulations (MC-GPU code) and a ray-tracing algorithm was employed for labeling the training data. The architectures of the neural networks are based on the XNet and multilayer perceptron, adapted for each task. The network predictions were compared with the ground truth using the coefficient of determination (r2). Results: The results have shown a good agreement for inner breast segmentation (r2 = 0.999), breast volume prediction (r2 = 0.982) and VGF prediction (r2 = 0.935). Moreover, the DgN coefficients using the predicted VGF for the virtual population differ on average 1.3% from the ground truth values. Afterwards with the obtained DgN coefficients, the MGD values were estimated from exposure factors extracted from the DICOM header of a clinical cohort, with median(75 percentile) values of 1.91(2.45) mGy. Conclusion: We successfully implemented a deep learning framework for VGF and MGD calculations for virtual breast phantoms.

PHYSICA MEDICA-EUROPEAN JOURNAL OF MEDICAL PHYSICS 83, 264-277, 2021. DOI: 10.1016/j.ejmp.2021.03.007

[P129-2021] "Coherence of oscillations in matter and supernova neutrinos"

Porto-Silva, Y. P.*; Smirnov, A. Y.

By harnessing quantum phenomena, quantum devices have the potential to outperform their classical counterparts. Here, we examine using wave function symmetry as a resource to enhance the performance of a quantum Otto engine. Previous work has shown that a bosonic working medium can yield better performance than a fermionic medium. We expand upon this work by incorporating a singular interaction that allows the effective symmetry to be tuned between the bosonic and fermionic limits. In this framework, the particles can be treated as anyons subject to Haldane's generalized exclusion statistics. Solving the dynamics analytically using the framework of "statistical anyons", we explore the interplay between interparticle interactions and wave function symmetry on engine performance.

JOURNAL OF COSMOLOGY AND ASTROPARTICLE PHYSICS [6], 029, 2021. DOI 10.1088/1475-7516/2021/06/029

[P130-2021] "Controlling Movement at Nanoscale: Curvature Driven Mechanotaxis"

Machado, L. D.; Bizao, R. A.; Pugno, N. M.; Galvao, D. S.*

Locating and manipulating nano-sized objects to drive motion is a time and effort consuming task. Recent advances show that it is possible to generate motion without direct intervention, by embedding the source of motion in the system configuration. In this work, an alternative manner to controllably displace nano-objects without external manipulation is demonstrated,

by employing spiral-shaped carbon nanotube (CNT) and graphene nanoribbon structures (GNR). The spiral shape contains smooth gradients of curvature, which lead to smooth gradients of bending energy. It is shown that these gradients as well as surface energy gradients can drive nano-oscillators. An energy analysis is also carried out by approximating the carbon nanotube to a thin rod and how torsional gradients can be used to drive motion is discussed. For the nanoribbons, the role of layer orientation is also analyzed. The results show that motion is not sustainable for commensurate orientations, in which AB stacking occurs. For incommensurate orientations, friction almost vanishes, and in this instance, the motion can continue even if the driving forces are not very high. This suggests that mild curvature gradients, which can already be found in existing nanostructures, could provide mechanical stimuli to direct motion.

SMALL, 2100909, 2021. DOI 10.1002/smll.202100909

[P131-2021] "Conversion of ferritin ferrihydrite core to magnetite by gold ions binding and the derived nanoparticle formation"

Tofanello, A.; Bronzato, J. D.; **Rettori, C.***; Nascimento, O. R.; Nantes-Cardoso, I. L.

Inspired by the multi-functionalities of vegetal extracts, we first focused on developing a new gold nanoparticle (AuNP) synthesis method using tomato extract (Solanum lycopersicum Mill, Carmen variety) under conditions in which proteins could be preserved and unexpected additional synthesis of superparamagnetic magnetite occurred. The AuNPs and magnetite were characterized by UV-visible spectroscopy, dynamic light scattering, superconducting quantum interference device, high-resolution transmission microscopy and energy-dispersive X-ray spectroscopy. Based on the literature, the ferrihydrite core of holoferritin was postulated to be the magnetite precursor. Consistently, the tomato genome encodes a protein homologous to ferritin and an identical result was obtained with purified horse spleen ferritin (HSF). The electron paramagnetic resonance spectrum of the lyophilized tomato pulp extract at 298 K featured HSF signal with (g(0) = 2.070). This signal is absent in another tomato variety (Solanum lycopersicum, cherry variety), as well as in the boiled Carmen tomato extract, which produced only AuNPs after stirring with HAu-Cl4. The synthesis of magnetite in an air atmosphere is feasible only using holoferritin because the synthesis by loading apoferritin with iron salt requires an inert atmosphere and controlled stoichiometry. In addition, AuNPs produced by this method exhibited potential for use in photodynamic therapy.

JOURNAL OF NANOSTRUCTURE IN CHEMISTRY 2021. DOI 10.1007/s40097-021-00423-8. Acesso antecipado.

[P132-2021] "Dark Energy Survey Year 3 results: Curved-sky weak lensing mass map reconstruction"

Jeffrey, N.; Gatti, M.; Navarro-Alsina, A.*; et al. DES Collaboration

We present reconstructed convergence maps, mass maps, from the Dark Energy Survey (DES) third year (Y3) weak gravitational lensing data set. The mass maps are weighted projections of the density field (primarily dark matter) in the foreground of the observed galaxies. We use four reconstruction methods, each is a maximum a posteriori estimate with a different model for the prior probability of the map: Kaiser-Squires, null B-mode prior, Gaussian prior, and a sparsity prior. All methods are implemented on the celestial sphere to accommodate the large sky coverage of the DES Y3 data. We compare the methods using realistic Lambda CDM simulations with mock data that are closely matched to the DES Y3 data.

We quantify the performance of the methods at the map level and then apply the reconstruction methods to the DES Y3 data, performing tests for systematic error effects. The maps are compared with optical foreground cosmic-web structures and are used to evaluate the lensing signal from cosmic-void profiles. The recovered dark matter map covers the largest sky fraction of any galaxy weak lensing map to date.

MONTHLY NOTICES OF THE ROYAL ASTRONOMICAL SOCIETY **505**[3], **4626-4645**, **136446**, **2021**. **DOI** 10.1093/mnras/ stab1495

[P133-2021] "Dark energy survey year 3 results: weak lensing shape catalogue"

Gatti, M.; Sheldon, E.; Navarro-Alsina, A.*; et al. DES Collaboration

We present and characterize the galaxy shape catalogue from the first 3 yr of Dark Energy Survey (DES) observations, over an effective area of 4143 deg(2) of the southern sky. We describe our data analysis process and our self-calibrating shear measurement pipeline METACALIBRATION, which builds and improves upon the pipeline used in the DES Year 1 analysis in several aspects. The DES Year 3 weak-lensing shape catalogue consists of 100 204 026 galaxies, measured in the riz bands, resulting in a weighted source number density of n(eff) = 5.59 gal arcmin(-2) and corresponding shape noise sigma(e) = 0.261. We perform a battery of internal null tests on the catalogue, including tests on systematics related to the point spread function (PSF) modelling, spurious catalogue B-mode signals, catalogue contamination, and galaxy properties.

MONTHLY NOTICES OF THE ROYAL ASTRONOMICAL SOCIETY 504[3], 4312-4336, 2021. DOI: 10.1093/mnras/stab918

[P134-2021] "Design, upgrade and characterization of the silicon photomultiplier front-end for the AMIGA detector at the Pierre Auger Observatory"

Aab, A.; Abreu, P.; Chinellato, J. A.*; Franco, D. de O.*; Dobrigkeit, C.*; Fauth, A. C.*; Payeras, A. M.*; Muller, M. A.*; et al. Pierre Auger Collaboration

AMIGA (Auger Muons and Infill for the Ground Array) is an upgrade of the Pierre Auger Observatory to complement the study of ultra-high-energy cosmic rays (UHECR) by measuring the muon content of extensive air showers (EAS). It consists of an array of 61 water Cherenkov detectors on a denser spacing in combination with underground scintillation detectors used for muon density measurement. Each detector is composed of three scintillation modules, with 10 m(2) detection area per module, buried at 2.3 m depth, resulting in a total detection area of 30 m(2). Silicon photomultiplier sensors (SiPM) measure the amount of scintillation light generated by charged particles traversing the modules. In this paper, the design of the front--end electronics to process the signals of those SiPMs and test results from the laboratory and from the Pierre Auger Observatory are described. Compared to our previous prototype, the new electronics shows a higher performance, higher efficiency and lower power consumption, and it has a new acquisition system with increased dynamic range that allows measurements closer to the shower core. The new acquisition system is based on the measurement of the total charge signal that the muonic component of the cosmic ray shower generates in the detector.

JOURNAL OF INSTRUMENTATION 16[1], P01026, 2021. DOI: 10.1088/1748-0221/16/01/P01026

[P135-2021] "Development of a new zinc oxide/tin oxide/carbon xerogel photocatalyst for visible light photodegradation of 4-chlorophenol"

Moraes, N. P. de; Goes, C. M.; Sperandio, D. C.; Rocha, R. D. da S.; Landers, R.*; Paramasivam, T.; Rodrigues, L. A.

This paper reports the development of a new carbon xerogel/ zinc oxide/tin oxide ternary photocatalyst and its application for the enhancement of photocatalytic response through the formation of heterojunctions composed of different phases. The results obtained from X-ray diffractometry showed that all the materials exhibited the hexagonal structure of zinc oxide. The application of infrared spectroscopy, energy dispersive spectroscopy and X-ray photoelectron spectroscopy (XPS) analyses helped confirm the presence of tin oxide and carbon xerogel in the photocatalytic material developed in the study. All the materials evaluated in the study showed photocatalytic activity under both solar and visible radiations. Under visible light, the optimized ternary material displayed higher photoactivity for 4-chlorophenol degradation, with total degradation of 55% in 5 h. The results obtained from chronoamperometry tests showed that the ternary composite exhibited the highest photocurrent among the samples evaluated when the materials were subjected to solar radiation.

MATERIALS SCIENCE AND ENGINEERING B-ADVANCED FUNCTIONAL SOLID-STATE MATERIALS 269, 115183, 2021. DOI: 10.1016/j.mseb.2021.115183

[P136-2021] "Development of a schwarzite-based moving bed 3D printed water treatment system for nanoplastic remediation"

Gupta, B.; Ambekar, R. S.; **Tromer, R. M.***; Ghosal, P. S.; Sinha, R.; Majumder, A.; Kumbhakar, P.; Ajayan, P. M.; **Galvao, D. S.***; Gupta, A. K.; Tiwary, C. S.

The impact of micro and nanoplastic debris on our aquatic ecosystem is among the most prominent environmental challenges we face today. In addition, nanoplastics create significant concern for environmentalists because of their toxicity and difficulty in separation and removal. Here we report the development of a 3D printed moving bed water filter (M-3DPWF), which can perform as an efficient nanoplastic scavenger. The enhanced separation of the nanoplastics happens due to the creation of a charged filter material that traps the more surface charged nanoparticles selectively. Synthetic contaminated water from polycarbonate waste has been tested with the filter, and enhanced nanoplastic removal has been achieved. The proposed filtration mechanism of surface-charge based water cleaning is further validated using density function theory (semi-empirical) based simulation. The filter has also shown good structural and mechanical stability in both static and dynamic water conditions. The field suitability of the novel treatment system has also been confirmed using water from various sources, such as sea, river, and pond. Our results suggest that the newly developed water filter can be used for the removal of floating nanoparticles in water as a robust advanced treatment system.

RSC ADVANCES 11[32], 19788-19796, 2021. DOI: 10.1039/d1ra03097c

[P137-2021] "EEG Signal Connectivity for Characterizing Interictal Activity in Patients With Mesial Temporal Lobe Epilepsy"

Costa, L. R. da*; Campos, B. M. de; Alvim, M. K. M.; Castellano, G.*

Over the last decade, several methods for analysis of epileptiform signals in electroencephalography (EEG) have been proposed. These methods mainly use EEG signal features in either the time or the frequency domain to separate regular, interictal, and ictal brain activity. The aim of this work was to evaluate the feasibility of using functional connectivity (FC) based feature extraction methods for the analysis of epileptiform discharges in EEG signals. These signals were obtained from EEG-fMRI sessions of 10 patients with mesial temporal lobe epilepsy (MTLE) with unilateral hippocampal atrophy. The connectivity functions investigated were motif synchronization, imaginary coherence, and magnitude squared coherence in the alpha, beta, and gamma bands of the EEG. EEG signals were sectioned into 1-s epochs and classified according to (using neurologist markers): activity far from interictal epileptiform discharges (IED), activity immediately before an IED and, finally, mid-IED activity. Connectivity matrices for each epoch for each FC function were built, and graph theory was used to obtain the following metrics: strength, cluster coefficient, betweenness centrality, eigenvector centrality (both local and global), and global efficiency. The statistical distributions of these metrics were compared among the three classes, using ANOVA, for each FC function. We found significant differences in all global (p < 0.001) and local (p < 0.00002) graph metrics of the far class compared with before and mid for motif synchronization on the beta band; local betweenness centrality also pointed to a degree of lateralization on the frontotemporal structures. This analysis demonstrates the potential of FC measures, computed using motif synchronization, for the characterization of epileptiform activity of MTLE patients. This methodology may be helpful in the analysis of EEG-fMRI data applied to epileptic foci localization. Nonetheless, the methods must be tested with a larger sample and with other epileptic phenotypes.

FRONTIERS IN NEUROLOGY 12, 673559, 2021. DOI 10.3389/fneur.2021.673559

[P138-2021] "Electron and photon reconstruction and identification with the CMS experiment at the CERN LHC"

Sirunyan, A. M; Tumasyan, A.; Chinellato, J. A.*; Tonelli Manganote, E. J.*; et al. CMS Collaboration

The performance is presented of the reconstruction and identification algorithms for electrons and photons with the CMS experiment at the LHC. The reported results are based on proton-proton collision data collected at a center-of-mass energy of 13 TeV and recorded in 2016-2018, corresponding to an integrated luminosity of 136 fb(-1). Results obtained from lead-lead collision data collected at root S-NN = 5.02 TeV are also presented. Innovative techniques are used to reconstruct the electron and photon signals in the detector and to optimize the energy resolution. Events with electrons and photons in the final state are used to measure the energy resolution and energy scale uncertainty in the recorded events. The measured energy resolution for electrons produced in Z boson decays in proton-proton collision data ranges from 2 to 5%, depending on electron pseudorapidity and energy loss through bremsstrahlung in the detector material. The energy scale in the same range of energies is measured with an uncertainty smaller than 0.1 (0.3)% in the barrel (endcap) region in proton-proton collisions and better than 1(3)% in the barrel (endcap) region in heavy ion collisions. The timing resolution for electrons from Z boson decays with the full 2016-2018 proton-proton collision data set is measured to be 200 ps.

JOURNAL OF INSTRUMENTATION 16[5], P05014, 2021. DOI 10.1088/1748-0221/16/05/P05014

[P139-2021] "Elliptic Flow of Electrons from Beauty-Hadron Decays in Pb-Pb Collisions at root s(NN)=5.02 TeV"

Acharya, S.; Adamova, D.; Albuquerque, D. S. D.*; Chinellato, D. D.*; Takahashi, J.*; et al. ALICE Collaboration

The elliptic flow of electrons from beauty hadron decays at midrapidity (vertical bar y vertical bar < 0.8) is measured in Pb-Pb collisions at root s(NN) = 5.02 TeV with the ALICE detector at the LHC. The azimuthal distribution of the particles produced in the collisions can be parametrized with a Fourier expansion, in which the second harmonic coefficient represents the elliptic flow, v(2). The v(2) coefficient of electrons from beauty hadron decays is measured for the first time in the transverse momentum (p(T)) range 1.3- 6 GeV/c in the centrality class 30%-50%. The measurement of electrons from beauty-hadron decays exploits their larger mean proper decay length c tau approximate to 500 mu m compared to that of charm hadrons and most of the other background sources. The v(2) of electrons from beauty hadron decays at midrapidity is found to be positive with a significance of 3.75 sigma. The results provide insights into the degree of thermalization of beauty quarks in the medium. A model assuming full thermalization of beauty quarks is strongly disfavored by the measurement at high p(T), but is in agreement with the results at low p(T). Transport models including substantial interactions of beauty quarks with an expanding strongly interacting medium describe the measurement within uncertainties.

PHYSICAL REVIEW LETTERS 126[16], 162001, 2021. DOI: 10.1103/PhysRevLett.126.162001

[P140-2021] "Enhancement of diamagnetism by momentummomentum interaction: Application to benzene"

Trevisan, T. V.*; Monteiro, G. M.*; Caldeira, A. O.*

Resumo: A well-known property of aromatic molecules is their highly anisotropic response to an external magnetic field: the magnetic susceptibility parallel to the field is generally much larger than the in-plane components. This intriguing phenomenon is rationalized as a consequence of the delocalization of the itinerant electrons that populate the aromatic ring. In this work, we revisit the magnetism of aromatic molecules and show that if the interaction between the itinerant and bonding electrons is taken into account, a large enhancement of the molecule magnetic response takes place. The itinerant electrons are described by an extended Hubbard Hamiltonian with an effective momentum-momentum interaction between them which is mediated by the bonding electrons. For the particular case of a benzene molecule, our model reproduces the experimentally observed magnetic anisotropy.

PHYSICAL REVIEW B 103[18], 180402, 2021. DOI: 10.1103/ PhysRevB.103.L180402

[P141-2021] "First measurement of the vertical bar t vertical bar-dependence of coherent J/psi photonuclear production"

Acharya, S.; Acosta, F. T.; Albuquerque, D. S. D.*; Chinellato, D. D.*; Souza, R. D. de*; Takahashi, J.*; et al. Alice Collaboration

The first measurement of the cross section for coherent J/Psi photoproduction as a function of vertical bar t vertical bar, the square of the momentum transferred between the incoming and outgoing target nucleus, is presented. The data were measured with the ALICE detector in ultra-peripheral Pb-Pbcollisions at a centre-of-mass energy per nucleon pair root s(NN) = 5.02 TeV with the J/Psi produced in the central rapidity region vertical bar y vertical bar < 0.8, which corresponds to the small Bjorken-xrange (0.3 - 1.4) x 10(-3). The measured vertical bar t vertical bar-dependence is not described by computations based only on the Pb nuclear form factor,

while the photonuclear cross section is better reproduced by models including shadowing according to the leading-twist approximation, or gluon-saturation effects from the impact-parameter dependent Balitsky-Kovchegov equation. These new results are therefore a valid tool to constrain the relevant model parameters and to investigate the transverse gluonic structure at very low Bjorken- x.

Physics Letters B 817, 136280, 2021. DOI: 10.1016/j.physle-tb.2021.136280

[P142-2021] "General Method for Classicality Certification in the Prepare and Measure Scenario"

Gois, C. de*; Moreno, G.; Nery, R.; Brito, S.; Chaves, R.; Rabelo, R.*

Preparing and measuring physical systems are the operational building blocks of any physical experiment, and to describe them is the first purpose of any physical theory. Remarkably, even when only uncharacterized preparation and measurement devices are present, it is sometimes possible to distinguish between the behaviors of quantum and classical systems from only observational data. Certifying the physical origin of measurement statistics in the prepare and measure scenario is of primal importance for developing quantum networks, distributing quantum keys, and certifying randomness, to mention a few applications, but, surprisingly, no general methods to do so are known. We progress on this problem by crafting a general, sufficient condition to certify that a given set of preparations can only generate classical statistics, for any number of generalized measurements. As an application, we employ the method to demonstrate nonclassicality activation in the prepare and measure scenario, also considering its application in random access codes. Following that, we adapt our method to certify, again through a sufficient condition, whether a given set of measurements can never give rise to nonclassical behaviors, irrespective of what preparations they may act upon. This, in turn, allows us to find a large set of incompatible measurements that cannot be used to demonstrate nonclassicality, thus showing incompatibility is not sufficient for nonclassicality in the prepare and measure scenario.

PRX QUANTUM 2[3], 030311, 2021. DOI 10.1103/PRXQuantum2.030311

[P143-2021] "Hearing brain evaluated using near-infrared spectroscopy in congenital toxoplasmosis"

Bertachini, A. L. L.; Januario, G. C.; Novi, S. L.*; Mesquita, R. C.*; Silva, M. A. R.; Andrade, G. M. Q.; Resende, L. M. de; Miranda, D. M. de

Congenital toxoplasmosis (CT) is a known cause of hearing loss directly caused by Toxoplasma gondii. Hearing loss might result from sensory, neural, or sensorineural lesions. Early treated infants rarely develop hearing loss, but retinochoroidal lesions, intracranial calcifications and hydrocephalus are common. In this study, we aimed to evaluate the brain evoked hemodynamic responses of CT and healthy infants during four auditory stimuli: mother infant directed speech, researcher infant directed speech, mother reading and researcher recorded. Children underwent Transitionally Evoked Otoacoustic Emission Auditory Testing and Automated Brainstem Auditory Response tests with normal auditory results, but with a tendency for greater latencies in the CT group compared to the control group. We assessed brain hemodynamics with functional near-infrared spectroscopy (fNIRS) measurements from 61 infants, and we present fNIRS results as frequency maps of activation and deactivation for each stimulus.

By evaluating infants in the three first months of life, we observed an individual heterogeneous brain activation pattern in response to all auditory stimuli for both groups. Each channel was activated or deactivated in less than 30% of children for all stimuli. There is a need of prospective studies to evaluate if the neurologic or auditory changes course with compromise of children outcomes.

SCIENTIFIC REPORTS 11[1], 10135, 2021. DOI: 10.1038/s41598-021-89481-0

[P144-2021] "High Electrical Anisotropic Multilayered Self-Assembled Organic Films Based on Graphene Oxide and PEDOT:PSS"

Gaal, G.*; Braunger, M. L.*; Rodrigues, V.*; Riul, A.*; Gomes, H. L.

Multilayered self-assembled structures having different constituents are very appealing for preparing novel materials with unusual electrical phenomena not observed on the individual sheets. Here, the fabrication and characterization of aligned multilayered architectures comprised of reduced graphene oxide (rGO) and poly(3,4-ethylenedioxythiophene) polystyrene sulfonate (PEDOT:PSS), embedded into polymer electrolytes, are reported. The in-plane conductivity is five orders of magnitude higher than the cross-plane value, resulting in the highest anisotropic ratio reported to date for multilayer materials. Temperature-dependent measurements corroborate the high anisotropic electrical behavior, with charge transport weakly thermally activated (E-a = 33 meV) along the aligned conductive phases. Cross-plane charge transport fits well with the variable ranging hopping model, presenting an activation energy of 1.0 eV. Such a high anisotropic electrical behavior is explored in a novel transistor architecture where the anisotropic film operates simultaneously as a dielectric layer and as a transistor channel, with the cross-plane electric field modulating the in-plane conduction. The device shows ambipolar charge transport; however, the n-type carrier transport dominates the conduction with the field-effect mobility of 4.0 cm(2) V-1 s(-1). A simple and efficient way is presented to use electrical anisotropy to tailor transistors without a lattice mismatch at the dielectric/semiconductor interface.

ADVANCED ELECTRONIC MATERIALS 7[8], 2100255, 2021. DOI: 10.1002/aelm.202100255 (Artigo destaque de capa)

[P145-2021] "High-field specific heat and entropy obtained from adiabatic temperature change"

Paixao, L. S.*; Usuda, E. O.; Imamura, W.; Carvalho, A. M. G.

Specific heat and entropy are relevant thermodynamic properties, which may be used as macroscopic probes to microscopic properties of materials under ambient conditions and under high applied fields. However, the measurement of specific heat under intense external fields can be a challenging task, as well as to obtain the entropy in the same conditions. Here, we describe a method to obtain high-field specific heat and entropy from measurements of specific heat under ambient conditions and direct temperature change induced by adiabatic field changes. We derive straightforward thermodynamic equations to calculate the specific heat and entropy, and our results agree satisfactorily with experimental data of specific heat under magnetic field, electric field, and pressure.

EUROPEAN PHYSICAL JOURNAL PLUS 136[5], 545, 2021. DOI: 10.1140/epjp/s13360-021-01538-1

[P146-2021] "High-frequency GMI hysteresis effect analysis by first-order reversal curve (FORC) method"

Arzuza, L. C. C.*; Beron, F.*; Pirota, K. R.*

In this work, we investigate the giant magnetoimpedance (GMI) hysteresis at high-frequency (10 MHz & ndash; 1 GHz) of Co-based amorphous magnetic ribbons. The first-order reversal curve (FORC) method was used to analyze their hysteretic behavior present at a low magnetic field (below 7 Oe). Results show that the GMI hysteresis is related to both the system magnetic anisotropy and the current frequency (through the skin depth). The GMI hysteresis gradually decreases upon frequency increase before disappearing, while a clockwise rotation of the FORC distributions is observed. These results are attributed to a heterogeneous magnetic structure in the magnetic ribbon volume. On the other side, while the cut-off frequency depends on the magnetic anisotropy strength, an inverted GMI hysteresis revives for the higher anisotropy ribbon. Above this frequency inversion, FORC results indicate a hardening of the effective switching field as a thicker region is probed. We propose that in this case, the stronger perpendicular anisotropy creates important differences between the superficial and volumetric anisotropy, enough to induce interaction between the two regions of different magnetization directions. This sensitive FORC protocol can be applied for investigating the GMI hysteresis, and thus the complex magnetic structure of several soft magnetic systems.

JOURNAL OF MAGNETISM AND MAGNETIC MATERIALS 534, 168008, 2021. DOI: 10.1016/j.jmmm.2021.168008

[P147-2021] "Hydrogen bonding arrangement of ice II observed in interfacial water attached on hydrophobic and hydrophilic surfaces"

Teschke, O.*; Castro, J. R. de*; Gomes, W. E.; Soares, D. M.*

Interfacial water dielectric permittivity and electric field profiles were probed and compared. Relative permittivity values between 3 and 4 were measured on both hydrophobic and hydrophilic substrates. Since ice has crystal structures responsible for many of the liquid water properties, Raman spectral lines of ice II were compared to the intramolecular vibrational spectrum of the interfacial air/water region. The coincidence of their spectral lines suggests that the interfacial air/water arrangement is similar to ice II and is induced by the interfacial electric field.

CHEMICAL PHYSICS LETTERS 775, 138655, 2021. DOI: 10.1016/j.cplett.2021.138655

[P148-2021] "Hyperfine couplings as a probe of orbital anisotropy in heavy-fermion materials"

Menegasso, P.*; Souza, J. C.*; Vinograd, I.; Wang, Z.; Edwards, S. P.; Pagliuso, P. G.*; Curro, N. J.; Urbano, R. R.*

Overlap between neighboring atomic wave functions is a central feature of conducting solids. In heavy-fermion materials, f-electron orbitals in the lattice lie on the boundary between fully localized and hybridized in an energy band. This dichotomy gives rise to a range of behaviors, including antiferromagnetism, unconventional superconductivity, and the ability to tune from one ground state to the other continuously. Measuring the degree of this hybridization by traditional methods is challenging and indirect. We utilize an approach using NMR to determine the magnetic couplings between the f electrons and neighboring nuclear spins in a series of CeRh1-xIrxIn5 crystals and find that the hybridization is strongly direction dependent in this important class of superconducting heavy-fermion materials. Our results demonstrate that hyperfine coupling measurements provide a quantitative measure of orbital anisotropy.

PHYSICAL REVIEW B 104[3], 035154, 2021. DOI 10.1103/ PhysRevB.104.035154

[P149-2021] "Impact of Inclined Lorentz Force and Schmidt Number on Chemically Reactive Newtonian Fluid Flow on a Stretchable Surface When Stefan Blowing and Thermal Radiation are Significant"

Mahabaleshwar, U. S.; Anusha, T.; Sakanaka, P. H.*; Bhatta-charyya, S.

The influence of inclined magnetic field and heat and mass transfer of a hydromagnetic fluid on stretching/shrinking sheet with Stefan blowing effects and radiation has been investigated. The elementary viscous equations for momentum, heat and mass transfer, which are highly nonlinear partial differential equations, are mapped into highly nonlinear ordinary differential equations with the help of similarity transformation. The subsequent highly nonlinear differential equation is solved analytically. The exact solution of heat and mass transfer appearances is found in terms of the incomplete gamma function. The species and temperature boundary conditions are assumed to be a linear function of the distance from the origin. Further, the impact of various parameters, such as Chandrasekhar number, thermal radiation, inclined Lorentz force and mass transpiration on velocity and temperature summaries, are conferred in detail.

ARABIAN JOURNAL FOR SCIENCE AND ENGINEERING número 208, 2021. DOI 10.1007/s13369-021-05976-y Acesso antecipado

[P150-2021] "Impact of photoelectric cross section data on systematic uncertainties for Monte Carlo breast dosimetry in mammography"

Massera, R. T.*; Fernandez-Varea, J. M.; Tomal, A.*

Monte Carlo (MC) simulations are employed extensively in breast dosimetry studies. In the energy interval of interest in mammography energy deposition is predominantly caused by the photoelectric effect, and the corresponding cross sections used by the MC codes to model this interaction process have a direct influence on the simulation results. The present work compares two photoelectric cross section databases in order to estimate the systematic uncertainty, related to breast dosimetry, introduced by the choice of cross sections for photoabsorption. The databases with and without the so-called normalization screening correction are denoted as 'renormalized' or 'un-normalized', respectively. The simulations were performed with the PENELOPE/penEasy code system, for a geometry resembling a mammography examination. The mean glandular dose (MGD), incident air kerma (K (air)), normalized glandular dose (DgN) and glandular depth-dose (GDD(z)) were scored, for homogeneous breast phantoms, using both databases. The AAPM Report TG-195 case 3 was replicated, and the results were included. Moreover, cases with heterogeneous and anthropomorphic breast phantoms were also addressed. The results simulated with the un-normalized cross sections are in better overall agreement with the TG-195 data than those from the renormalized cross sections; for MGD the largest discrepancies are 0.13(6)% and 0.74(5)%, respectively. The MGD, K (air) and DgN values simulated with the two databases show differences that diminish from approximately 10%/3%/6.8% at 8.25 keV down to 1.5%/1.7%/0.4% at 48.75 keV, respectively. For polyenergetic spectra, deviations up to 2.5% were observed. The disagreement between the GDDs simulated with the analyzed databases increases with depth, ranging from -1% near the breast entrance to 4% near the bottom. Thus, the choice of photoelectric cross section database affects the MC simulation results of breast dosimetry and adds a non-negligible systematic uncertainty to the dosimetric quantities used in mammography.

PHYSICS IN MEDICINE AND BIOLOGY 66[11], 115015, 2021. DOI: 10.1088/1361-6560/abf859

[P151-2021] "In-medium modification of dijets in PbPb collisions at root s(NN)=5.02 TeV"

Sirunyan, A. M.; Tumasyan, A.; Chinellato, J. A.*; Tonelli Manganote, E. J.*; et al. CMS Collaboration

Modifications to the distribution of charged particles with respect to high transverse momentum (p(T)) jets passing through a quark-gluon plasma are explored using the CMS detector. Back-to-back dijets are analyzed in lead-lead and proton--proton collisions at root s(NN) = 5.02 TeV via correlations of charged particles in bins of relative pseudorapidity and angular distance from the leading and subleading jet axes. In comparing the lead-lead and proton-proton collision results, modifications to the charged-particle relative distance distribution and to the momentum distributions around the jet axis are found to depend on the dijet momentum balance x(j), which is the ratio between the subleading and leading jet p(T). For events with x(i) approximate to 1, these modifications are observed for both the leading and subleading jets. However, while subleading jets show significant modifications for events with a larger dijet momentum imbalance, much smaller modifications are found for the leading jets in these events.

JOURNAL OF HIGH ENERGY PHYSICS [5], 116, 2021. DOI: 10.1007/JHEP05(2021)116

[P152-2021] "Inclusive heavy-flavour production at central and forward rapidity in Xe-Xe collisions at , root sNN=5.44 TeV"

Acharya, S.; Adamova, D.; Albuquerque, D. S. D.*; Chinellato, D. D.*; Takahashi, J.*; et al. ALICE Collaboration

The first measurements of the production of muons and electrons from heavy-flavour hadron decays in Xe-Xe collisions at root s(NN) = 5.44 TeV, using the ALICE detector at the LHC, are reported. The measurement of the nuclear modification factor RAA is performed as a function of transverse momentum pT in several centrality classes at forward rapidity (2.5 < y < 4) and midrapidity (vertical bar y vertical bar < 0.8) for muons and electrons from heavy-flavour hadron decays, respectively. A suppression by a factor up to about 2.5 compared to the binary-scaled pp reference is observed in central collisions at both central and forward rapidities. The RAA of muons from heavy-flavour hadron decays is compared to previous measurements in Pb-Pb collisions at root sNN = 5.02 TeV. When the nuclear modification factors are compared in the centrality classes 0-10% for Xe-Xe collisions and 10-20% for Pb-Pb collisions, which have similar charged-particle multiplicity density, a similar suppression, with R-AA similar to 0.4 in the p(T) interval 4 < p(T) < 8 GeV/c, is observed. The comparison of the measured R-AA values in the two collision systems brings new insights on the properties of the quark-gluon plasma by investigating the system-size and geometry dependence of medium-induced parton energy loss. The results of muons and electrons from heavy-flavour hadron decays provide new constraints to model calculations.

PHYSICS LETTERS B 819, 136437, 2021. DOI 10.1016/j.physletb.2021.136437

[P153-2021] "Infrared facets of the three-gluon vertex"

Aguilar, A. C.*; Soto, F. De; **Ferreira, M. N.***; Papavassiliou, J.; Rodriguez-Quintero, J.

We present novel lattice results for the form factors of the quenched three-gluon vertex of QCD, in two special kinematic configurations that depend on a single momentum scale. We consider three form factors, two associated with a classical tensor structure and one without tree-level counterpart, exhibiting markedly different infrared behaviors. Specifically, while the former display the typical suppression driven by a negative logarithmic singularity at the origin, the latter saturates at a small negative constant. These exceptional features are analyzed within the Schwinger-Dyson framework, with the aid of special relations obtained from the Slavnov-Taylor identities of the theory. The emerging picture of the underlying dynamics is thoroughly corroborated by the lattice results, both qualitatively as well as quantitatively.

PHYSICS LETTERS B 818, 136352, 2021. DOI: 10.1016/j.physletb.2021.136352

[P154-2021] "Interaction generalisation and demographic feedbacks drive the resilience of plant-insect networks to extinctions"

Maia, K. P.; Marquitti, F. M. D.*; Vaughan, I. P.; Memmott, J.; Raimundo, R. L. G.

Understanding the processes driving ecological resilience, that is the extent to which systems retain their structure while absorbing perturbations, is a central challenge for theoretical and applied ecologists. Plant-insect assemblages are well-suited for the study of ecological resilience as they are species-rich and encompass a variety of ecological interactions that correspond to essential ecosystem functions. Mechanisms affecting community response to perturbations depend on both the natural history and structure of ecological interactions. Natural history attributes of the interspecific interactions, for example whether they are mutualistic or antagonistic, may affect the ecological resilience by controlling the demographic feedbacks driving ecological dynamics at the community level. Interaction generalisation may also affect resilience, by defining opportunities for interaction rewiring, the extent to which species are able to switch interactions in fluctuating environments. These natural history attributes may also interact with network structure to affect ecological resilience. Using adaptive network models, we investigated the resilience of plant-pollinator and plant-herbivore networks to species loss. We specifically investigated how fundamental natural history differences between these systems, namely the demographic consequences of the interaction and their level of generalisation-mediating rewiring opportunities-affect the resilience of dynamic ecological networks to extinctions. We also create a general benchmark for the effect of network structure on resilience simulating extinctions on theoretical networks with controlled structures. When network structure was static, pollination networks were less resilient than herbivory networks; this is related to their high levels of nestedness and the reciprocally positive feedbacks that define mutualisms, which made co-extinction cascades more likely and longer in plant-pollinator assemblages. When considering interaction rewiring, the high generalisation and the structure of pollination networks boosted their resilience to extinctions, which approached those of herbivory networks. Simulation results using theoretical networks suggested that the empirical structure of herbivory networks may protect them from collapse. Elucidating the ecological and evolutionary processes driving interaction rewiring is key to understanding the resilience of plant-insect assemblages. Accounting for rewiring requires ecologists to combine natural history with network models that incorporate feedbacks between species abundances, traits and interactions. This combination will elucidate how perturbations propagate at community level, reshaping biodiversity structure and ecosystem functions.

JOURNAL OF ANIMAL ECOLOGY Article Number 136280,2021. DOI: 10.1111/1365-2656.13547 Acesso antecipado

[P155-2021] "Jet-associated deuteron production in pp collisions at root s=13 TeV"

Acharya, S.; Adamova, D.; Albuquerque, D. S. D.*; Chinellato, D. D.*; Takahashi, J.*; et al. ALICE Collaboration

Deuteron production in high-energy collisions is sensitive to the space-time evolution of the collision system, and is typically described by a coalescence mechanism. For the first time, we present results on jet-associated deuteron production in pp collisions at root s=13 TeV, providing an opportunity to test the established picture for deuteron production in events with a hard scattering. Using a trigger particle with high transverse-momentum (p(T) > 5 GeV/c) as a proxy for the presence of a jet at midrapidity, we observe a measurable population of deuterons being produced around the jet proxy. The associated deuteron yield measured in a narrow angular range around the trigger particle differs by 2.4-4.8 standard deviations from the uncorrelated background. The data are described by PYTHIA model calculations featuring baryon coalescence.

PHYSICS LETTERS B 819, 136440. 2021. DOI 10.1016/j.physletb.2021.136440

[P156-2021] "Laser cooling with three-level cascade transitions: a study for group II atoms and ytterbium"

Magno, W. C.; Cruz, F. C.*

We analyze laser cooling of two-electron atoms with three-level cascade transitions, involving the usual S-1(0)-P-1(1) cooling transition coupled to either S-1(0) or D-1(2) states. We numerically calculate minimum temperatures for the most abundant even isotopes of group II atoms and ytterbium (which lack hyperfine structure), derive general analytical expressions from a perturbative approach, and discuss the experimental implementation of the technique. Considered as an alternative 2nd stage technique to intercombination line cooling, three-level cooling is clearly advantageous for light elements, such as Mg and Ca, while for all elements provides much higher capture ranges, increasing the transfer efficiency from the 1st stage cooling, with faster cooling times and sub-Doppler temperatures.

JOURNAL OF PHYSICS B-ATOMIC MOLECULAR AND OPTICAL PHYSICS 54[14], 145301, 2021. DOI 10.1088/1361-6455/abf8a0

[P157-2021] "Layered metal halide perovskite solar cells: A review from structure-properties perspective towards maximization of their performance and stability"

Holanda, M. S. de*; Moral, R. F.; Marchezi, P. E.; Marques, F. C.*; Nogueira, A. F.

Perovskite solar cells (PSCs) technology is now reaching its full potential in terms of power conversion efficiency, but still presenting problems related to long-term stability under operating conditions. One of the most promising alternatives to PSCs is the layered PSCs (2D-PSCs). Layered perovskites present a huge compositional variety, which can be used to directly tune photophysical characteristics that influence the operational mechanisms of the devices. This review addresses the structural organization of both the organic and inorganic sublattices, focusing on how the structure influences the quantum and dielectric confinement, phonons and charge carriers' dynamics, charge mobility, and structural defects. We discuss the relation between the structure-properties of layered perovskites with the performance of solar cells. We, then, offer insights into how these characteristics have been controlled in the assembly of 2D-PSCs to improve their efficiency and stability.

We conclude by giving a perspective of future developments and open areas of exploration that might impact the progress of this rapidly growing technology.

ECOMAT Article Number L011901, 2021. DOI 10.1002/eom2.12124 Acesso antecipado

[P158-2021] "Measurement of differential t(t)over-bar production cross sections using top quarks at large transverse momenta in pp collisions at root s=13 TeV"

Sirunyan, A. M.; Tumasyan, A.; Chinellato, J. A.*; Manganote, E. J. Tonelli*; et al. CMS Collaboration

A measurement is reported of differential top quark pair (t (t) over bar) production cross sections, where top quarks are produced at large transverse momenta. The data collected with the CMS detector at the LHC are from pp collisions at a center--of-mass energy of 13 TeV corresponding to an integrated luminosity of 35.9 fb(-1). The measurement uses events where at least one top quark decays as t -> Wb -> qq(-1)b and is reconstructed as a large-radius jet with transverse momentum in excess of 400 GeV. The second top quark is required to decay either in a similar way or leptonically, as inferred from a reconstructed electron or muon, a bottom quark jet, and missing transverse momentum due to the undetected neutrino. The cross section is extracted as a function of kinematic variables of individual top quarks or of the t (t) over bar system. The results are presented at the particle level, within a region of phase space close to that of the experimental acceptance, and at the parton level and are compared to various theoretical models. In both decay channels, the observed absolute cross sections are significantly lower than the predictions from theory, while the normalized differential measurements are well described.

PHYSICAL REVIEW D 103[5], 052008, 2021. DOI: 10.1103/ PhysRevD.103.052008

[P159-2021] "Measurement of the azimuthal anisotropy of Y(1S) and Y(2S) mesons in PbPb collisions at root s(NN)=5.02 TeV"

Sirunyan, A. M.; Tumasyan, A.; Chinellato, J. A.*; Manganote, E. J. Tonelli*; et al. CMS Collaboration

The second-order Fourier coefficients (v(2)) characterizing the azimuthal distributions of Y(1S) and Y(2S) mesons produced in PbPb collisions at root s(NN) = 5.02 TeV are studied. The Y mesons are reconstructed in their dimuon decay channel, as measured by the CMS detector. The collected data set corresponds to an integrated luminosity of 1.7 nb(-1). The scalar product method is used to extract the v2 coefficients of the azimuthal distributions. Results are reported for the rapidity range vertical bar y vertical bar < 2.4, in the transverse momentum interval 0 < pT < 50 GeV/c, and in three centrality ranges of 10-30%, 30-50% and 50-90%. In contrast to the J/psi mesons, the measured v(2) values for the Y mesons are found to be consistent with zero.

PHYSICS LETTERS B 819, 136385, 2021. DOI 10.1016/j.physletb.2021.136385

[P160-2021] "Measurement of the Fluctuations in the Number of Muons in Extensive Air Showers with the Pierre Auger Observatory"

Aab, A.; Abreu, P.; Chinellato, J. A.*; Franco, D. de O.*; Dobrigkeit, C.*; Fauth, A. C.*; Payeras, A. M.*; Muller, M. A.*; et al. Pierre Auger Collaboration

We present the first measurement of the fluctuations in the number of muons in extensive air showers produced by ultrahigh energy cosmic rays. We find that the measured fluctuations are in good agreement with predictions from air shower simulations. This observation provides new insights into the origin of the previously reported deficit of muons in air shower simulations and constrains models of hadronic interactions at ultrahigh energies. Our measurement is compatible with the muon deficit originating from small deviations in the predictions from hadronic interaction models of particle production that accumulate as the showers develop.

PHYSICAL REVIEW LETTERS 126[15], 152002, 2021. DOI: 10.1103/PhysRevLett.126.152002

[P161-2021] "Measurement of the W gamma Production Cross Section in Proton-Proton Collisions at root s=13 TeV and Constraints on Effective Field Theory Coefficients"

Sirunyan, A. M.; Tumasyan, A.; Chinellato, J. A.*; et al. CMS Collaboration

A fiducial cross section for W gamma production in proton-proton collisions is measured at a center-of-mass energy of 13 TeV in 137 fb(-1) of data collected using the CMS detector at the LHC. The W -> e nu and mu nu decay modes are used in a maximum-likelihood fit to the lepton-photon invariant mass distribution to extract the combined cross section. The measured cross section is compared with theoretical expectations at next-to-leading order in quantum chromodynamics. In addition, 95% confidence level intervals are reported for anomalous triple-gauge couplings within the framework of effective field theory.

PHYSICAL REVIEW LETTERS 126[25], 252002, 2021. DOI 10.1103/PhysRevLett.126.252002

[P162-2021] "Measurement of the Z boson differential production cross section using its invisible decay mode (Z -> nu(nu)over-bar) in proton-proton collisions at root s=13 TeV

Sirunyan, A. M.; Tumasyan, A.; Chinellato, J. A.*; Tonelli Manganote, E. J.*; et al. CMS Collaboration

Measurements of the total and differential fiducial cross sections for the Z boson decaying into two neutrinos are presented at the LHC in proton-proton collisions at a center-of-mass energy of 13TeV. The data were collected by the CMS detector in 2016 and correspond to an integrated luminosity of 35.9 fb(-1). In these measurements, events are selected containing an imbalance in transverse momentum and one or more energetic jets. The fiducial differential cross section is measured as a function of the Z boson transverse momentum. The results are combined with a previous measurement of charged-lepton decays of the Z boson. The measured total fiducial cross section for events with Z boson transverse momentum greater than 200 GeV is 3000(-170)(+180) fb.

JOURNAL OF HIGH ENERGY PHYSICS [5], 205, 2021. DOI: 10.1007/JHEP05(2021)205

[P163-2021] "Measurements of Higgs boson production cross sections and couplings in the diphoton decay channel at root s=13 TeV"

Sirunyan, A. M.; Tumasyan, A.; Chinellato, J. A.*; Tonelli Manganote, E. J.* et al. CMS Collaboration

Measurements of Higgs boson production cross sections and couplings in events where the Higgs boson decays into a pair of photons are reported.

Events are selected from a sample of proton-proton collisions at root s = 13TeV collected by the CMS detector at the LHC from 2016 to 2018, corresponding to an integrated luminosity of 137 fb(-1). Analysis categories enriched in Higgs boson events produced via gluon fusion, vector boson fusion, vector boson associated production, and production associated with top quarks are constructed. The total Higgs boson signal strength, relative to the standard model (SM) prediction, is measured to be 1.12 +/- 0.09. Other properties of the Higgs boson are measured, including SM signal strength modifiers, production cross sections, and its couplings to other particles. These include the most precise measurements of gluon fusion and vector boson fusion Higgs boson production in several different kinematic regions, the first measurement of Higgs boson production in association with a top quark pair in five regions of the Higgs boson transverse momentum, and an upper limit on the rate of Higgs boson production in association with a single top quark. All results are found to be in agreement with the SM expectations.

JOURNAL OF HIGH ENERGY PHYSICS [7], 027, 2021. DOI 10.1007/JHEP07(2021)027

[P164-2021] "Measurements of mixed harmonic cumulants in Pb-Pb collisions at root s(NN)=5.02 TeV"

Acharya, S.; Adamova, D.; Chinellato, D. D.*; Guardiano, G. G.*; Jahnke, C.*; Takahashi, J.*; et al. ALICE Collaboration

Correlations between moments of different flow coefficients are measured in Pb-Pb collisions at root s(NN) = 5.02 TeV recorded with the ALICE detector. These new measurements are based on multiparticle mixed harmonic cumulants calculated using charged particles in the pseudorapidity region vertical bar eta vertical bar < 0.8 with the transverse momentum range 0.2 < p(T) < 5.0 GeV/c. The centrality dependence of correlations between two flow coefficients as well as the correlations between three flow coefficients, both in terms of their second moments, are shown. In addition, a collection of mixed harmonic cumulants involving higher moments of v(2) and v(3) is measured for the first time, where the characteristic signature of negative, positive and negative signs of four-, six- and eight--particle cumulants are observed, respectively. The measurements are compared to the hydrodynamic calculations using iE-BE-VISHNU with AMPT and TRENTo initial conditions. It is shown that the measurements carried out using the LHC Run 2 data in 2015 have the precision to explore the details of initial-state fluctuations and probe the nonlinear hydrodynamic response of v(2) and v(3) to their corresponding initial anisotropy coefficients epsilon(2) and epsilon(3). These new studies on correlations between three flow coefficients as well as correlations between higher moments of two different flow coefficients will pave the way to tighten constraints on initial-state models and help to extract precise information on the dynamic evolution of the hot and dense matter created in heavy-ion collisions at the LHC.

PHYSICS LETTERS B 818, 136354, 2021. DOI: 10.1016/j.physletb.2021.136354

[P165-2021] "Measurements of production cross sections of the Higgs boson in twhe four-lepton final state in protonproton collisions at root s=13 TeV"

Sirunyan, A. M.; Tumasyan, A.; Chinellato, J. A.*; et al. CMS Collaboration

Production cross sections of the Higgs boson are measured in the H -> ZZ -> 4l (l=e, mu) decay channel.A data sample of proton-proton collisions at a center-of-mass energy of 13 TeV, collected by the CMS detector at the LHC and corresponding to an integrated luminosity of 137 fb(-1) is used.

The signal strength modifier mu, defined as the ratio of the Higgs boson production rate in the 4l channel to the standard model (SM) expectation, is measured to be mu = 0.94 +/- 0.07 (stat) (-0.08)(+0.09) (syst) at a fixed value of m(H) = 125.38 GeV. The signal strength modifiers for the individual Higgs boson production modes are also reported. The inclusive fiducial cross section for the H -> 4l process is measured to be 2.84(-0.22)(+0.23) (stat)(-0.21)(+0.26) (syst) fb, which is compatible with the SM prediction of 2.84 +/- 0.15 fb for the same fiducial region. Differential cross sections as a function of the transverse momentum and rapidity of the Higgs boson, the number of associated jets, and the transverse momentum of the leading associated jet are measured. A new set of cross section measurements in mutually exclusive categories targeted to identify production mechanisms and kinematical features of the events is presented. The results are in agreement with the SM predictions.

EUROPEAN PHYSICAL JOURNAL C 81[6], 488, 2021. DOI: 10.1140/epjc/s10052-021-09200-x

[P166-2021] "Measurements of the differential cross sections of the production of Z plus jets and gamma plus jets and of Z boson emission collinear with a jet in pp collisions at root s=13 TeV"

Sirunyan, A. M.; Tumasyan, A.; Chinellato, J. A.*; Manganote, E. J. Tonelli*; et al. CMS Collaboration

Measurements of the differential cross sections of Z + jets and gamma + jets production, and their ratio, are presented as a function of the boson transverse momentum. Measurements are also presented of the angular distribution between the Z boson and the closest jet. The analysis is based on pp collisions at a center-of-mass energy of 13 TeV corresponding to an integrated luminosity of 35.9 fb(-1) recorded by the CMS experiment at the LHC. The results, corrected for detector effects, are compared with various theoretical predictions. In general, the predictions at higher orders in perturbation theory show better agreement with the measurements. This work provides the first measurement of the ratio of the differential cross sections of Z + jets and gamma + jets production at 13 TeV, as well as the first direct measurement of Z bosons emitted collinearly with a jet.

JOURNAL OF HIGH ENERGY PHYSICS [5], 285, 2021. DOI: 10.1007/JHEP05(2021)285

[P167-2021] "Mechanical properties of single-walled pentagraphene-based nanotubes: A DFT and Classical molecular dynamics study"

Sousa, J. M. De; Aguiar, A. L.; Girao, E. C.; Fonseca, A. F.*; Coluci, V. R.; Galvao, D. S.*

Membranes of carbon allotropes comprised solely of densely packed pentagonal rings, known as penta-graphene, exhibit negative Poisson's ratio (auxetic behavior) and a bandgap of 3.2 eV. In this work, we investigated the structural stability, mechanical and fracture properties of nanotubes formed by rolling up penta-graphene membranes, the so-called penta--graphene nanotubes (PGNTs). Single-walled PGNT of three distinct configurations: (n, 0), and two types of (n, n) (here called alpha and beta) were studied combining first-principles calculations and reactive molecular dynamics simulations. Our results showed Young's modulus values of 680-800 GPa, critical strain of 18-21%, ultimate tensile stress of 85-110 GPa, and Poisson's ratio values ranging from -0.05 to -0.30 (auxetic behavior). During stretching at room temperature, we observed a transition from beta-(n, n) to alpha-(n, n) PGNT near the critical strain. Fracture of PGNTs starts at the bonds that are mostly aligned to the stretching direction and after nanotube radial collapse.

CHEMICAL PHYSICS 547, 111187, 2021. DOI: 10.1016/j.chem-phys.2021.111187

[P168-2021] "Nonlinear charge transport in highly polar semiconductors: GaN, AlN, InN and GaAs"

Rodrigues, C. G.; Luzzi, R.*

In this paper, we present a collection of results focussing on the transport properties of doped direct-gap inverted-band highly polar III-nitride semiconductors (GaN, AlN, InN) and GaAs in the transient and steady state, calculated by using nonlinear quantum kinetic theory based on a non-equilibrium statistical ensemble formalism (NESEF). In the present paper, these results are compared with calculations using Monte Carlo modelling simulations and experimental measurements. Both n-type and p-type materials, in the presence of intermediate to high electric fields, are considered for several temperatures and carrier concentrations. The agreement between the results obtained using nonlinear quantum kinetic theory, with those of Monte Carlo calculations and experimental data is remarkably good, thus satisfactorily validating the NESEF.

PRAMANA-JOURNAL OF PHYSICS 95[1], 44, 2021. DOI 10.1007/s12043-021-02077-1

[P169-2021] "Nonlinear higher-order hydrodynamics: Fluids under driven flow and shear pressure"

Rodrigues, C. G.; Ramos, J. G.*; Silva, C. A. B.; Luzzi, R.*

In the context of a nonequilibrium statistical thermodynamics-based on a nonequilibrium statistical ensemble formalism-a generalized hydrodynamics of fluids under driven flow and shear stress is derived. At the thermodynamic level, the nonequilibrium equations of state are derived, which are coupled to the evolution of the basic variables that describe the hydrodynamic motion in such a system. Generalized diffusion-advection and Maxwell-Cattaneo advection equations are obtained in appropriate limiting situations. This nonlinear higher-order hydrodynamics is applied, in an illustration, to the case of a dilute solution of Brownian particles in nonequilibrium conditions and flowing in a solvent acting as a thermal bath. This is done in the framework of such generalized hydrodynamics but truncated up to a second order.

PHYSICS OF FLUIDS 33[6], 067111, 2021. DOI 10.1063/5.0047645

[P170-2021] "Observation of a New Excited Beauty Strange Baryon Decaying to Xi(-)(b)pi(+)pi(-)"

Sirunyan, A. M; Tumasyan, A.; Chinellato, J. A.*; et al. CMS Collaboration

The Xi(-)(b)pi(+)pi(-) invariant mass spectrum is investigated with an event sample of proton-proton collisions at root s = 13TeV, collected by the CMS experiment at the LHC in 2016-2018 and corresponding to an integrated luminosity of 140 fb(-1). The ground state Xi(-)(b) is reconstructed via its decays to J/ psi Xi(-) and J/psi Lambda K-. A narrow resonance, labeled Xi(b)(6100)(-), is observed at a Xi(-)(b)pi(+)pi(-) invariant mass of 6100.3 +/- 0.2(stat) +/- 0.1(syst) +/- 0.6(Xi(-)(b)) MeV, where the last uncertainty reflects the precision of the Xi(-)(b) baryon mass. The upper limit on the Xi(b)(6100)(-) natural width is determined to be 1.9 MeV at 95% confidence level. The low Xi(b)(6100)(-) signal yield observed in data does not allow a measurement of the quantum numbers of the new state. However, following analogies with the established excited Xi(c) baryon states, the new Xi(b)(6100)(-) resonance and its decay sequence are consistent with the orbitally excited Xi(-)(b) baryon, with spin and parity quantum numbers J(P) = 3/2(-).

PHYSICAL REVIEW LETTERS 126[25], 252003, 2021. DOI 10.1103/PhysRevLett.126.252003

[P171-2021] "Odd-frequency pair density wave in the Kitaev-Kondo lattice model"

Carvalho, V. S. de*; Teixeira, R. M. P.; Freire, H.; Miranda, E.*

We investigate the properties of the Kitaev-Kondo lattice model defined on a bilayer honeycomb lattice by means of the SO(3) Majorana representation for spin-1/2 moments. We first consider the pairing of neighboring sites for the parent Kitaev spin-liquid (KSL) Hamiltonian to render the Majorana and the spin-1/2 Hilbert spaces perfectly equivalent to each other. As a consequence, we demonstrate that this decoupling of the Kitaev interaction in terms of the SO(3) Majorana fermions reproduces exactly the spectrum of the KSL model alone. Then, by considering the effect of a local Kondo coupling J(K) in the model and decoupling it in terms of an order parameter that physically must have a finite staggering phase, we obtain that the system undergoes a quantum phase transition from a fractionalized Fermi liquid to a nematic triplet superconducting (SC) phase as J(K) is increased. Depending on the model parameters, this SC phase can exhibit either Dirac points, Bogoliubov-Fermi lines, or Bogoliubov-Fermi surfaces as nodal bulk manifolds. The surface states in this latter case are also characterized by topologically protected antichiral edge modes. The SC phase breaks time-reversal symmetry and exhibits a coexistence of a dominant odd-frequency pairing with a small even-frequency component for electronic excitations localized on sites of the same sublattice of the system. Finally, we show that this SC phase is in fact a pair-density-wave state, with Cooper pairs possessing a finite center-of-mass momentum in zero magnetic field.

PHYSICAL REVIEW B 103[17], 174512, 2021. DOI: 10.1103/ PhysRevB.103.174512

[P172-2021] "Osseointegration Improvement of Co-Cr-Mo Alloy Produced by Additive Manufacturing"

latecola, A.; Longhitano, G. A.; Antunes, L. H. M.; Jardini, A. L.; Miguel, E. de C.; Beres, M.; Lambert, C. S.*; Andrade, T. N.; Buchaim, R. L.; Buchaim, D. V.; Pomini, K. T.; Dias, J. A.; Spressao, D. R. M. S.; Felix, M.; Cardoso, G. B. C.; Cunha, M. R. da

Cobalt-base alloys (Co-Cr-Mo) are widely employed in dentistry and orthopedic implants due to their biocompatibility, high mechanical strength and wear resistance. The osseointegration of implants can be improved by surface modification techniques. However, complex geometries obtained by additive manufacturing (AM) limits the efficiency of mechanical-based surface modification techniques. Therefore, plasma immersion ion implantation (PIII) is the best alternative, creating nanotopography even in complex structures. In the present study, we report the osseointegration results in three conditions of the additively manufactured Co-Cr-Mo alloy: (i) as-built, (ii) after PIII, and (iii) coated with titanium (Ti) followed by PIII. The metallic samples were designed with a solid half and a porous half to observe the bone ingrowth in different surfaces. Our results revealed that all conditions presented cortical bone formation. The titanium-coated sample exhibited the best biomechanical results, which was attributed to the higher bone ingrowth percentage with almost all medullary canals filled with neoformed bone and the pores of the implant filled and surrounded by bone ingrowth. It was concluded that the metal alloys produced for AM are biocompatible and stimulate bone neoformation, especially when the Co-28Cr-6Mo alloy with a Ti-coated surface, nanostructured and anodized by PIII is used, whose technology has been shown to increase the osseointegration capacity of this implant.

PHARMACEUTICS 13[5], 724, 2021. DOI: 10.3390/pharmaceutics13050724

[P173-2021] "Oxygenation of Diamond Surfaces via Hummer's Method"

Puthirath, A. B.; Oliveira, E. F.*; Gao, G. H.; Chakingal, N.; Kannan, H.; Li, C. X.; Zhang, X.; Biswas, A.; Neupane, M. R.; Pate, B. B.; Ruzmetov, D. A.; Birdwell, A. G.; Ivanov, T. G.; Galvao, D. S.*; Vajtai, R.; Ajayan, P. M.

Oxygen bonded with diamond surfaces impacts important properties such as electrical conductivity, Schottky barrier height, field emission, and chemical reactivity. Though processes such as thermal, hydrogen plasma, etc., are efficient in oxidizing the hydrogen-terminated diamond surfaces, the oxidation of pristine diamond surfaces through wet chemical treatments is still in its infancy. Herein, we investigated the efficacy of Hummer's method, one of the most celebrated chemical oxidation procedures to convert graphite to graphene oxide, to oxidize the pristine diamond surfaces. We attempted to oxidize both microcrystalline diamond powders and polycrystalline diamond wafers. Due to the presence of an acidic oxidative environment and the formation of strong oxidizing agents such as Mn207 and Mn03+ during the course of the reaction, Hummer's method is found to be very effective in oxidizing the pristine diamond surfaces. The degree of oxygen termination is validated through various spectroscopic and surface probe measurements. Microcrystalline diamond powder is more prone to oxidation to polycrystalline diamond wafers due to excess surface area, and many facets with different dangling bond densities are exposed to the oxidizing medium. The experimental observations are endorsed through molecular dynamics simulations.

CHEMISTRY OF MATERIALS 33[13], 4977-4987, 145301, 2021. DOI 10.1021/acs.chemmater.1c00772

[P174-2021] "Prehydrodynamic evolution and its signatures in final-state heavy-ion observables"

Silva, T. N. da; Chinellato, D.*; Denicol, G. S.; Hippert, M.*; Luzum, M.; Noronha, J.; Serenone, W.*; Takahashi, J.* ExTrE-Me Collaboration

We investigate the effects of prehydrodynamic evolution on final-state observables in heavy-ion collisions using state-of-the art event simulations coupled to different prehydrodynamic scenarios, which include the recently developed effective kinetic transport theory evolution model Kempty setMPempty setST. Differential flow observables are found to be mostly insensitive to the details of prehydrodynamic evolution. The main effect we observe is in the P T spectra, particularly the mean transverse momentum. However, at least part of this effect is a consequence of the underlying conformal invariance assumption currently present in such approaches, which is known to be violated in the temperature regime probed in heavy-ion collisions. This assumption of early time conformal invariance leads to an artificially large out-of-equilibrium bulk pressure when switching from (conformal) prehydrodynamic evolution to hydrodynamics (using the nonconformal QCD equation of state), which in turn increases the transverse momentum. Our study indicates that a consistent treatment of prehydrodynamic evolution in heavy-ion collisions requires the use of nonconformal models of early time dynamics.

PHYSICAL REVIEW C 103[5], 054906, 2021. DOI: 10.1103/ PhysRevC.103.054906

[P175-2021] "Quantum criticality in a layered iridate"

Samanta, K.*; Souza, J. C.*; Rigitano, D.*; Morales, A. I.*; Pagliuso, P. G.*; Granado, E.*

Iridates provide a fertile ground to investigate correlated electrons in the presence of strong spin-orbit coupling.

Bringing these systems to the proximity of a metal-insulator quantum phase transition is a challenge that must be met to access quantum critical fluctuations with charge and spin-orbital degrees of freedom. Here, electrical transport and Raman scattering measurements provide evidence that a metal-insulator quantum critical point is effectively reached in 5% Co-doped Sr2IrO4 with high structural quality. The dc-electrical conductivity shows a linear temperature dependence that is successfully captured by a model involving a Co acceptor level at the Fermi energy that becomes gradually populated at finite temperatures, creating thermally-activated holes in the J(eff)=1/2 lower Hubbard band. The so-formed quantum critical fluctuations are exceptionally heavy and the resulting electronic continuum couples with an optical phonon at all temperatures. The magnetic order and pseudospin-phonon coupling are preserved under the Co doping. This work brings quantum phase transitions, iridates and heavy-fermion physics to the same arena. Due to a combination of strong spin orbit coupling and electron correlations iridates such as Sr2IrO4 exhibit a range of exotic quantum states that can be tuned via their electronic and magnetic properties. Here, the authors investigate the resistive and Raman scattering properties of Co-doped Sr2IrO4 and provide evidence for quantum critical fluctuations in the system.

COMMUNICATIONS PHYSICS 4[1], 89, 2021. DOI: 10.1038/s42005-021-00591-7

[P176-2021] "Quantum Euler Relation for Local Measurements"

Touil, A.; Weber, K.; Deffner, S.*

In classical thermodynamics the Euler relation is an expression for the internal energy as a sum of the products of canonical pairs of extensive and intensive variables. For quantum systems the situation is more intricate, since one has to account for the effects of the measurement back action. To this end, we derive a quantum analog of the Euler relation, which is governed by the information retrieved by local quantum measurements. The validity of the relation is demonstrated for the collective dissipation model, where we find that thermodynamic behavior is exhibited in the weak-coupling regime.

ENTROPY 23[7], 889, 2021. DOI 10.3390/e23070889

[P177-2021] "Quantum Heat Engines with Singular Interactions"

Myers, N. M.; McCready, J.; Deffner, S.*

By harnessing quantum phenomena, quantum devices have the potential to outperform their classical counterparts. Here, we examine using wave function symmetry as a resource to enhance the performance of a quantum Otto engine. Previous work has shown that a bosonic working medium can yield better performance than a fermionic medium. We expand upon this work by incorporating a singular interaction that allows the effective symmetry to be tuned between the bosonic and fermionic limits. In this framework, the particles can be treated as anyons subject to Haldane's generalized exclusion statistics. Solving the dynamics analytically using the framework of "statistical anyons", we explore the interplay between interparticle interactions and wave function symmetry on engine performance.

SYMMETRY-BASEL 13[6], 978, 2021. DOI 10.3390/sym13060978

[P178-2021] "Reducible oxide and allotropic transition induced by hydrogen annealing: synthesis routes of TiO2 thin films to tailor optical response"

Echeverrigaray, F. G.*; Zanatta, A. R.; Alvarez, F.*

Optical properties of hydrogenated TiO2 thin films deposited by the ion beam sputtering method are reported. By reducing the oxide by hydrogenation in situ (during deposition) and ex situ (by means of posterior thermal annealing) a controlled phase modification allows to manipulate optical properties to improve photoactivity for solar energy conversion and catalytic applications. The hydrogenation procedure prompts remarkable structural changes and optical properties of the TiO2 hierarchical thin films. Photoemission electron spectroscopy (XPS) results show the presence of titanium in Ti4+ into Ti3+ state of oxidation, i.e., compatible with oxygen vacancies and titanium interstitials. Vibrational properties inspected by IR absorption and Raman spectroscopy allowed identifying potentially catalytic sites and vibration modes associated with hydrogen. The vibrational spectra show that both in situ and ex situ hydrogenation routes contribute to prompt (dis)order in the films, involving the presence of anatase crystalline phase embedded in an amorphous matrix or mixed-phase (anatase rutile) crystalline TiO2. To avoid debate about the TiO2 theoretical (indirect) and expected and measured (direct, normally reported) optical gap (E-gap), the absorption coefficient spectra were analyzed by a recently developed method based on the Boltzmann sigmoidal function. From these analyses, conclusions about defects states prompted by the hydrogenation processes are presented.

JOURNAL OF MATERIALS RESEARCH AND TECHNOLOGY-JMR&T 12, 1623-1637, 2021. DOI: 10.1016/j.jmrt.2021.03.082

[P179-2021] "Resolving the LMA-dark NSI degeneracy with coherent neutrino-nucleus scattering"

Chaves, M.*; Schwetz, T.

In the presence of non-standard neutrino interactions (NSI), a degeneracy exists in neutrino oscillation data, which involves the flipping of the octant of the mixing angle theta (12) and the type of the neutrino mass ordering. In this article, we revisit the status of this degeneracy in the light of recent data on coherent elastic neutrino-nucleus scattering (CE nu NS) from the COHERENT experiment. For general relative couplings to up and down quarks, the degeneracy is disfavoured at the 2 sigma level by the latest data but remains at a higher confidence level. We investigate the requirements of future CE nu NS measurements to resolve the degeneracy with high significance. We find that a measurement involving both, electron and muon neutrino flavours and a target with a neutron-to-proton ratio close to 1 is required. For example, an experiment with a silicon target at the European Spallation Source can resolve the degeneracy at more than 4 sigma for arbitrary relative couplings to up and down quarks.

JOURNAL OF HIGH ENERGY PHYSICS [5], 42, 2021. DOI: 10.1007/JHEP05(2021)042

[P180-2021] "Robust Narrow-Gap Semiconducting Behavior in Square-Net La3Cd2As6"

Piva, M. M.*; Rahn, M. C.; Thomas, S. M.; Scott, B. L.; **Pagliuso, P. G.***; Thompson, J. D.; Schoop, L. M.; Ronning, F.; Rosa, P. F. S.

Narrow-gap semiconductors are sought-after materials due to their potential for long-wavelength detectors, thermoelectrics, and more recently nontrivial topology. Here, we report the synthesis and characterization of a new family of narrow-gap semiconductors, R3Cd2As6 (R = La and Ce). Single-crystal X-ray diffraction at room temperature reveals that the As square nets distort and Cd vacancies order in a monoclinic superstructure. A putative charge-density ordered state sets in at 279 K in La-3Cd2As6 and at 136 K in Ce3Cd2As6 and is accompanied by a substantial increase in the electrical resistivity in both compounds.

The resistivity of the La member increases by 13 orders of magnitude on cooling, which points to a remarkably clean semiconducting ground state. Our results suggest that light square-net materials within an 14/mmm parent structure are promising clean narrow-gap semiconductors.

CHEMISTRY OF MATERIALS 33[11], 136280, 4122-4127, 2021. DOI: 10.1021/acs.chemmater.1c00797

[P181-2021] "Scalable Synthesis of Atomically Thin Gallium Telluride Nanosheets for Supercapacitor Applications"

Siddique, S.; Gowda, C. C.; **Tromer, R.***; Demiss, S.; Gautam, A. R. S.; Femi, O. E.; Kumbhakar, P.; **Galvao, D. S.***; Chandra, A.; Tiwary, C. S.

An easily scalable fabrication method has been explored to obtain atomically thin gallium telluride (GaTe), which opens up new prospective applications of this well-known material. Due to nanostructuring, the optical and electrochemical properties of 2D GaTe at room temperature see remarkable improvements. The effects of surface defects on the optical properties have also been demonstrated. The performance of atomically thin GaTe as a supercapacitor is investigated. It shows a significantly high specific capacitance, 14 F g(-1) (without additive/composite forms). As a function of cycling, exfoliated GaTe exhibits similar to 96% charge retention (10 000 cycles), confirming high material stability. H/H-2 adsorption studies using density functional theory (DFT) calculations show that the defects in 2D GaTe impart the desired properties. Hence, 2D GaTe is useful in storage device applications and also as a stable electrode material. DFT simulations were also used to gain insights into the semiconducting behavior of the material, which can be utilized to tune the electrochemical and optical properties.

ACS APPLIED NANO MATERIALS 4[5], 4829-4838, 2021. DOI: 10.1021/acsanm.1c00428

[P182-2021] "Sciatic nerve regeneration after traumatic injury using magnetic targeted adipose-derived mesenchymal stem cells"

Soto, P. A.; Vence, M.; Pinero, G. M.; Coral, D. F.; Usach, V.; Muraca, D.*; Cueto, A.; Roig, A.; van Raap, M. B. F.; Setton-Avruj, C. P.

Traumatic peripheral nerve injuries constitute a huge concern to public health. Nerve damage leads to a decrease or even loss of mobility of the innervated area. Adult stem cell therapies have shown some encouraging results and have been identified as promising treatment candidates for nerve regeneration. A major obstacle to that approach is securing a sufficient number of cells at the injured site to produce measurable therapeutic effects. The present work tackles this issue and demonstrates enhanced nerve re-generation ability promoted by magnetic targeted cell therapy in an in vivo Wallerian degeneration model. To this end, adipose-derived mesenchymal stem cells (Ad-MSC) were loaded with citric acid coated super-paramagnetic iron oxide nanoparticles (SPIONs), systemically transplanted and magnetically recruited to the injured sciatic nerve. AdMSC arrival to the injured nerve was significantly increased using magnetic targeting and their beneficial effects surpassed the regenerative properties of the stand-alone cell therapy. Ad-MSC-SPIONs group showed a partially conserved nerve structure with many intact myelinated axons. Also, a very remarkable restoration in myelin basic protein organization, indicative of remyelination, was observed. This resulted in an improvement in nerve conduction, demonstrating functional recovery. In summary, our results demonstrate that magnetically assisted delivery of AdMSC, using a non-invasive and non-traumatic method, is a highly promising strategy to promote cell recruitment and sciatic nerve regeneration after traumatic injury.

Last but not least, our results validate magnetic targeting in vivo ex-ceeding previous reports in less complex models through cell magnetic targeting in vitro and ex vivo. Statement of significance Traumatic peripheral nerve injuries constitute a huge public health concern. They can lead to a decrease or even loss of mobility of innervated areas. Due to their complex pathophysiology, current pharmaco-logical and surgical approaches are only partially effective. Cell-based therapies have emerged as a useful tool to achieve full tissue regeneration. However, a major bottleneck is securing enough cells at injured sites. Therefore, our proposal combining biological (adipose derived mesenchymal stem cells) and nan-otechnological strategies (magnetic targeting) is of great relevance, reporting the first in vivo experiments involving "magnetic stem cell" targeting for peripheral nerve regeneration. Using a non-invasive and non traumatic method, cell recruitment in the injured nerve was improved, fostering nerve remyelination and functional recovery.

ACTA BIOMATERIALIA 130, 234-247, 086101, 2021. DOI 10.1016/j.actbio.2021.05.050

[P183-2021] "Search for long-lived particles using displaced jets in proton-proton collisions at root s=13 TeV"

Sirunyan, A. M; Tumasyan, A.; Chinellato, J. A.*; Tonelli Manganote, E. J.*; et al. CMS Collaboration

An inclusive search is presented for long-lived particles using displaced jets. The search uses a data sample collected with the CMS detector at the CERN LHC in 2017 and 2018, from proton-proton collisions at a center-of-mass energy of 13 TeV. The results of this search are combined with those of a previous search using a data sample collected with the CMS detector in 2016, yielding a total integrated luminosity of 132 fb(-1). The analysis searches for the distinctive topology of displaced tracks and displaced vertices associated with a dijet system. For a simplified model, where pair-produced long-lived neutral particles decay into guark-antiquark pairs, pair production cross sections larger than 0.07 fb are excluded at 95% confidence level (C.L.) for long-lived particle masses larger than 500 GeV and mean proper decay lengths between 2 and 250 mm. For a model where the standard model--like Higgs boson decays to two long-lived scalar particles that each decays to a quark-antiquark pair, branching fractions larger than 1% are excluded at 95% C.L. for mean proper decay lengths between 1 mm and 340 mm. A group of supersymmetric models with pair-produced long-lived gluinos or top squarks decaying into various final-state topologies containing displaced jets is also tested. Gluino masses up to 2500 GeV and top squark masses up to 1600 GeV are excluded at 95% C.L. for mean proper decay lengths between 3 and 300 mm. The highest lower bounds on mass reach 2600 GeV for long-lived gluinos and 1800 GeV for long-lived top squarks. These are the most stringent limits to date on these models.

PHYSICAL REVIEW D 104[1], 012015, 2021. DOI 10.1103/ PhysRevD.104.012015

[P184-2021] "Search for resonant and nonresonant new phenomena in high-mass dilepton final states at root s=13 TeV"

Sirunyan, A. M.; Tumasyan, A.; Chinellato, J. A.*; Tonelli Manganote, E. J.*; et al. CMS Collaboration

A search is presented for physics beyond the standard model (SM) using electron or muon pairs with high invariant mass. A data set of proton-proton collisions collected by the CMS experiment at the LHC at root s = 13 TeV from 2016 to 2018 corresponding to a total integrated luminosity of up to 140 fb(-1) is analyzed. No significant deviation is observed with respect to the SM background expectations.

Upper limits are presented on the ratio of the product of the production cross section and the branching fraction to dileptons of a new narrow resonance to that of the Z boson. These provide the most stringent lower limits to date on the masses for various spin-1 particles, spin-2 gravitons in the Randall-Sundrum model, as well as spin-1 mediators between the SM and dark matter particles. Lower limits on the ultraviolet cutoff parameter are set both for four-fermion contact interactions and for the Arkani-Hamed, Dimopoulos, and Dvali model with large extra dimensions. Lepton flavor universality is tested at the TeV scale for the first time by comparing the dimuon and dielectron mass spectra. No significant deviation from the SM expectation of unity is observed.

JOURNAL OF HIGH ENERGY PHYSICS [7], 208, 2021. DOI 10.1007/JHEP07(2021)208

[P185-2021] "Search for singly and pair-produced leptoquarks coupling to third-generation fermions in proton-proton collisions at root s=13 TeV"

Sirunyan, A. M; Tumasyan, A.; Chinellato, J. A.*; Tonelli Manganote, E. J.*; et al. CMS Collaboration

A search for leptoquarks produced singly and in pairs in proton-proton collisions is presented. We consider the leptoquark (LQ) to be a scalar particle of charge -1/3e coupling to a top quark plus a tau lepton (t tau) or a bottom quark plus a neutrino (b nu), or a vector particle of charge +2/3e, coupling to t nu or b tau. These choices are motivated by models that can explain a series of anomalies observed in the measurement of B meson decays. In this analysis the signatures t tau nu b and t tau nu are probed, using data recorded by the CMS experiment at the CERN LHC at root s = 13 TeV and that correspond to an integrated luminosity of 137 fb(-1). These signatures have not been previously explored in a dedicated search. The data are found to be in agreement with the standard model prediction. Lower limits at 95% confidence level are set on the LQ mass in the range 0.98-1.73 TeV, depending on the LQ spin and its coupling lambda to a lepton and a quark, and assuming equal couplings for the two LQ decay modes considered. These are the most stringent constraints to date on the existence of leptoquarks in this scenario.

PHYSICS LETTERS B 819, 136446, 2021. DOI 10.1016/j.physletb.2021.136446

[P186-2021] "Search for the rare decay of the W boson into a pion and a photon in proton-proton collisions at root s=13 TeV"

Sirunyan, A. M; Tumasyan, A.; Chinellato, J. A.*; Tonelli Manganote, E. J.*; et al. CMS Collaboration

A search is performed for the rare decay W-+/--> pi(+/-)gamma in proton-proton collisions at root s = 13 TeV. Data corresponding to an integrated luminosity of 137 fb(-1) were collected during 2016 to 2018 with the CMS detector. This analysis exploits a novel search strategy based on W boson production in top quark pair events. An inclusive search for the W-+/--> pi(+/-)gamma decay is not optimal at the LHC because of the high trigger thresholds. Instead, a trigger selection is exploited in which the W boson originating from one of the top quarks is used to tag the event in a leptonic decay. The W boson emerging from the other top quark is used to search for the W-+/--> pi(+/-)gamma signature. Such decays are characterized by an isolated track pointing to a large energy deposit, and by an isolated photon of large transverse momentum. The presence of b quark jets reduces the background from the hadronization of light-flavor quarks and gluons. The W-+/- -> pi(+/-)gamma decay is not observed. An upper exclusion limit is set to this branching fraction, corresponding to 1.50 x 10(-5) at 95% confidence level,

whereas the expected upper exclusion limit is 0.85(-0.29) (+0.52) x 10(-5).

PHYSICS LETTERS B 819, 136409, 2021. DOI 10.1016/j.physletb.2021.136409

[P187-2021] "Soft-Dielectron Excess in Proton-Proton Collisions at root s=13 TeV"

Acharya, S.; Adamova, D.; Albuquerque, D. S. D.*; Chinellato, D. D.*; Takahashi, J.*; et al. Large Ion Collider Expt Collaborat

A measurement of dielectron production in proton-proton (pp) collisions at root s = 13 TeV, recorded with the ALICE detector at the CERN LHC, is presented in this Letter. The data set was recorded with a reduced magnetic solenoid field. This enables the investigation of a kinematic domain at low dielectron (ee) invariant mass m(ee) and pair transverse momentum p(T,ee)that was previously inaccessible at the LHC. The cross section for dielectron production is studied as a function of m(ee), p(T,ee), and event multiplicity dNch=d.. The expected dielectron rate from hadron decays, called hadronic cocktail, utilizes a parametrization of the measured eta/pi(0) ratio in pp and proton-nucleus collisions, assuming that this ratio shows no strong dependence on collision energy at low transverse momentum. Comparison of the measured dielectron yield to the hadronic cocktail at 0.15 < m(ee) < 0.6 GeV/c(2) and for p(T,ee) < 0.4 GeV/c indicates an enhancement of soft dielectrons, reminiscent of the "anomalous" soft-photon and soft--dilepton excess in hadron-hadron collisions reported by several experiments under different experimental conditions. The enhancement factor over the hadronic cocktail amounts to 1.61 +/- 0.13(stat) +/- 0.17(syst, data) +/- 0.34osyst; cocktailTHORN in the ALICE acceptance. Acceptance-corrected excess spectra in mee and pT; ee are extracted and compared with calculations of dielectron production from hadronic bremsstrahlung and thermal radiation within a hadronic many-body approach.

PHYSICAL REVIEW LETTERS 127[4], 042302, 2021. DOI 10.1103/PhysRevLett.127.042302

[P188-2021] "Study of Drell-Yan dimuon production in proton-lead collisions at root s(NN)=8.16 TeV"

Sirunyan, A. M.; Tumasyan, A.; Chinellato, J. A.*; Tonelli Manganote, E. J.*; et al. CMS Collaboration

Differential cross sections for the Drell-Yan process, including Z boson production, using the dimuon decay channel are measured in proton-lead (pPb) collisions at a nucleon-nucleon centre-of-mass energy of 8.16 TeV. A data sample recorded with the CMS detector at the LHC is used, corresponding to an integrated luminosity of 173 nb(-1). The differential cross section as a function of the dimuon mass is measured in the range 15-600 GeV, for the first time in proton-nucleus collisions. It is also reported as a function of dimuon rapidity over the mass ranges 15-60 GeV and 60-120 GeV, and ratios for the p-going over the Pb-going beam directions are built. In both mass ranges, the differential cross sections as functions of the dimuon transverse momentum p(T), and of a geometric variable phi* are measured, where phi* highly correlates with p(T), but is determined with higher precision. In the Z mass region, the rapidity dependence of the data indicate a modification of the distribution of partons within a lead nucleus as compared to the proton case. The data are more precise than predictions based upon current models of parton distributions.

JOURNAL OF HIGH ENERGY PHYSICS [5], 182, 2021. DOI: 10.1007/JHEP05(2021)182

[P189-2021] "Supernova neutrino burst detection with the Deep Underground Neutrino Experiment"

Abi, B.; Acciarri, R.; Holanda, P. C. de*; Gelli, B.*; Guzzo, M. M.*; Kemp, E.*; Machado, A. A.*; Peres, O. L. G.*; Prakash, S.*; Reggiani-Guzzo, M.*; Segreto, E.*; Nunes, M. S.*; Forero, D. V.*; Souza, H. V. de*; et al. DUNE Collaboration

The Deep Underground Neutrino Experiment (DUNE), a 40-kton underground liquid argon time projection chamber experiment, will be sensitive to the electron-neutrino flavor component of the burst of neutrinos expected from the next Galactic core-collapse supernova. Such an observation will bring unique insight into the astrophysics of core collapse as well as into the properties of neutrinos. The general capabilities of DUNE for neutrino detection in the relevant few- to few-tens-of-MeV neutrino energy range will be described. As an example, DUNE's ability to constrain the nu(e) spectral parameters of the neutrino burst will be considered.

EUROPEAN PHYSICAL JOURNAL C 81[5], 423, 2021. DOI: 10.1140/epjc/s10052-021-09166-w

[P190-2021] "Surface excitations relaxation in the Kondo insulator Sm1-xGdxB6"

Souza, J. C.*; Konig, M.; Crivillero, M. V. A.; Malcolms, M. O.*; Urbano, R. R.*; Fisk, Z.; Rosa, P. F. S.; Pagliuso, P. G*; Wirth, S.; Sichelschmidt, J.

The interplay between nontrivial topological states of matter and strong electronic correlations is one of the most compelling open questions in condensed matter physics. Due to experimental challenges, there is an increasing desire to find more microscopic techniques to complement the results of more traditional experiments. In this work, we locally explore the Kondo insulator Sm1-xGdxB6 by means of electron spin resonance (ESR) of Gd3+ ions at low temperatures. Our analysis reveals that the Gd3+ ESR line shape shows an anomalous evolution as a function of temperature, wherein for highly dilute samples (x approximate to 0.0002) the Gd3+ ESR line shape changes from a localized ESR local moment character to a diffusive-like character. Upon manipulating the sample surface with a focused ion beam we demonstrate, in combination with electrical resistivity measurements, that the localized character of the Gd3+ ESR line shape is recovered by increasing the penetration of the microwave in the sample. This provides compelling evidence for the contribution of surface or near-surface excitations to the relaxation mechanism in the Gd3+ spin dynamics. Our work brings new insights into the importance of nontrivial surface excitations in ESR, opening new routes to be explored both theoretically and experimentally.

PHYSICAL REVIEW RESEARCH 3[3], 033016, 2021. DOI 10.1103/PhysRevResearch.3.033016

[P191-2021] "Systematic manipulation of the surface conductivity of SmB6"

Crivillero, M. V. A.; Koenig, M.; Souza, J. C.*; Pagliuso, P. G.*; Sichelschmidt, J.; Rosa, P. F. S.; Fisk, Z.; Wirth, S.

We show that the resistivity plateau of SmB6 at low temperature, typically taken as a hallmark of its conducting surface state, can systematically be influenced by different surface treatments. We investigate the effect of inflicting an increasing number of handmade scratches and microscopically defined focused ion beam-cut trenches on the surfaces of flux-grown Sm1-xGdxB6 with x = 0 and 0.0002. Both treatments increase the resistance of the low-temperature plateau, whereas the bulk resistance at higher temperatures largely remains unaffected.

Notably, the temperature at which the resistance deviates from the thermally activated behavior decreases with cumulative surface damage. These features are more pronounced for the focused ion beam treated samples, with the difference likely being related to the absence of microscopic defects such as subsurface cracks. Therefore, our method presents a systematic way of controlling the surface conductance.

PHYSICAL REVIEW RESEARCH 3[2], **023162**, **2021**. **DOI**: 10.1103/PhysRevResearch.3.023162

[P192-2021] "The first Hubble diagram and cosmological constraints using superluminous supernovae"

Inserra, C.; Sullivan, M.; Sobreira, F.*; et al. D.E.S. Collaboration

We present the first Hubble diagram of superluminous supernovae (SLSNe) out to a redshift of two, together with constraints on the matter density, Omega(M), and the dark energy equation-of-state parameter, w(equivalent to p/rho). We build a sample of 20 cosmologically useful SLSNe I based on light curve and spectroscopy quality cuts. We confirm the robustness of the peak-decline SLSN I standardization relation with a larger data set and improved fitting techniques than previous works. We then solve the SLSN model based on the above standardization via minimization of the chi(2) computed from a covariance matrix that includes statistical and systematic uncertainties. For a spatially flat Lambda cold dark matter (Lambda CDM) cosmological model, we find, with an rms of 0.27 mag for the residuals of the distance moduli. For a w(0)w(a) CDM cosmological model, the addition of SLSNe I to a 'baseline' measurement consisting of Planck temperature together with Type Ia supernovae, results in a small improvement in the constraints of w(0) and w(a) of 4 per cent. We present simulations of future surveys with 868 and 492 SLSNe I (depending on the configuration used) and show that such a sample can deliver cosmological constraints in a flat Lambda CDM model with the same precision (considering only statistical uncertainties) as current surveys that use Type Ia supernovae, while providing a factor of 2-3 improvement in the precision of the constraints on the time variation of dark energy, w(0) and w(a). This paper represents the proof of concept for superluminous supernova cosmology, and demonstrates they can provide an independent test of cosmology in the high-redshift (z > 1) universe.

MONTHLY NOTICES OF THE ROYAL ASTRONOMICAL SOCIETY 504[2], 2535-2549, 027, 2021. DOI 10.1093/mnras/stab978

[P193-2021] "The Lorentz-violating real scalar field at thermal equilibrium"

Aguirre, A. R.; Flores-Hidalgo, G.; Rana, R. G.; Souza, E. S.*

In this paper we study Lorentz-violation (LV) effects on the thermodynamics properties of a real scalar field theory due to the presence of a constant background tensor field. In particular, we analyse and compute explicitly the deviations of the internal energy, pressure, and entropy of the system at thermal equilibrium due to the LV contributions. For the free massless scalar field we obtain exact results, whereas for the massive case we perform approximated calculations. Finally, we consider the self interacting phi 4 theory, and perform perturbative expansions in the coupling constant for obtaining relevant thermodynamics quantities.

EUROPEAN PHYSICAL JOURNAL C 81[5], 459, 2021. DOI 10.1140/epjc/s10052-021-09250-1

[P194-2021] "Twisting or untwisting graphene twisted nanoribbons without rotation"

Fonseca, A. F.*

The common sense regarding twisting or untwisting a ribbon is that it requires the application of an external rotation to happen. However, at nanoscale, the application of precise amounts of rotation on a nanoribbon is not a trivial task. Here, the concept of an alternative method to add twist to or remove twist from a twisted graphene nanoribbon (TGNR) without rotation is presented and computationally demonstrated. The method consists of suspending a TGNR on two separate substrates and, by changing only their distance, the total amount of twist of the TGNR is shown to change. The possibility of fine-tuning the amount of twist of a TGNR is also shown. The concept is demonstrated through fully atomistic molecular dynamics simulations and numerical calculations of the topological parameters twist and writhe of a TGNR. It is shown that the above process satisfies the so--called linking number theorem of space curves. Besides being capable of precisely determining the total twist of a TGNR, this concept reveals a twist to writhe transition phenomenon that is tension-free and does not require controlling either the nanoribbon end-to-end distance or its critical twist density.

PHYSICAL REVIEW B 104[4], 045401, 2021. DOI 10.1103/Phys-RevB.104.045401

[P195-2021] "Two-Photon Polymerization: Functionalized Microstructures, Micro-Resonators, and Bio-Scaffolds"

Otuka, A. J. G.; Tomazio, N. B.*; Paula, K. T.; Mendonca, C. R.

The direct laser writing technique based on two-photon polymerization (TPP) has evolved considerably over the past two decades. Its remarkable characteristics, such as 3D capability, sub-diffraction resolution, material flexibility, and gentle processing conditions, have made it suitable for several applications in photonics and biosciences. In this review, we present an overview of the progress of TPP towards the fabrication of functionalized microstructures, whispering gallery mode (WGM) microresonators, and microenvironments for culturing microorganisms. We also describe the key physical-chemical fundamentals underlying the technique, the typical experimental setups, and the different materials employed for TPP.

POLYMERS 13[12], 1994, 2021. DOI: 10.3390/polym13121994

[P196-2021] "Understanding the Dependence of Nanoparticles Magnetothermal Properties on Their Size for Hyperthermia Applications: A Case Study for La-Sr Manganites"

Ferreira, M. C.; Pimentel, B.; Andrade, V.*; Zverev, V.; Gimaev, R. R.; Pomorov, A. S.; Pyatakov, A.; Alekhina, Y.; Komlev, A.; Makarova, L.; Perov, N.; Reis, M. S.

Magnetic oxides are promising materials for alternative health diagnoses and treatments. The aim of this work is to understand the dependence of the heating power with the nanoparticle (NP) mean size, for the manganite composition La0.75Sr0.25MnO3 (LSMO)-the one with maximum critical temperature for the whole La/Sr ratio of the series. We have prepared four different samples, each one annealed at different temperatures, in order to produce different mean NP sizes, ranging from 26 nm up to 106 nm. Magnetization measurements revealed a FC-ZFC irreversibility and from the coercive field as function of temperature we determined the blocking temperature. A phase diagram was delivered as a function of the NP mean size and, based on this, the heating mechanism understood.

Small NPs (26 nm) is heated up within the paramagnetic range of temperature (T>T-c), and therefore provide low heating efficiency; while bigger NPs are heated up, from room temperature, within the magnetically blocked range of temperature (TT>TB), for intermediate mean diameter size of 37 nm, with maximum efficiency of heat transfer.

NANOMATERIALS 11[7], 1826, 2021. DOI 10.3390/ nano11071826

[P197-2021] "Unveiling the Ag-Bi miscibility at the atomic level: A theoretical insight"

Anez, R.; Cabral, L.; Silva, E. Z. da*; Longo, E.; Andres, J.; San-Miguel, M. A.

Alloying metals that are not miscible at the solid bulk phase attracted great interest in the scientific community due to their distinctive electronic, optical, catalytic, and magnetic properties compared to pure metals. However, an in-depth understanding of the processes involved in forming these alloy materials is somewhat limited, especially at the atomic level. Density functional theory (DFT) calculations have been carried out to rationalize the formation of an Ag-Bi interface as a critical stage to the partial miscibility observed in recent experiments. Appropriate models of Ag-Bi nanostructures have been selected to determine the structural, electronic properties, and energetic changes along with the formation of nanoalloys. The calculated values of the segregation energy indicate that the interface plays a crucial role in stabilizing the Ag-doped with Bi atoms. The migration process of the Bi atoms from the Ag surface to the Ag bulk is favored. This process, which is difficult to occur on a clean surface due to the high density of the Ag cubic phase, has been revealed theoretically and confirmed experimentally. However, on clean Bi surfaces, the insertion of Ag atoms is probabilistically more favorable with concomitant structural changes of the cell parameters to form Ag-Bi bonds since the Bi surfaces are less compact and low symmetry.

COMPUTATIONAL MATERIALS SCIENCE 197, 110612, 2021. DOI 10.1016/j.commatsci.2021.110612

[P198-2021] "Visceral adipose tissue glucose uptake is linked to prognosis in multiple myeloma patients: An exploratory study"

Cunha, A. D. da; Silveira, M. N.; **Takahashi**, **M. E. S.***; Souza, E. M. de; Mosci, C.; Ramos, C. D.; Brambilla, S. R.; Pericole, F. V.; Prado, C. M.; Mendes, M. C. S.; Carvalheira, J. B. C.

Background & aims: The use of computerized tomography to opportunistically assess body composition has highlighted abnormalities such as low muscle mass and high adiposity may be hidden conditions in cancer patients. However, the role of skeletal muscle (SM), subcutaneous (SAT) and visceral (VAT) adipose tissue glucose uptake measured by 18F-fluorodeoxyglucose (18F-FDG) positron emission tomography (PET)-CT on patient prognostication is unclear. Methods: Patients with multiple myeloma (MM) with satisfactory image frame for assessing body composition and for semi-quantification of SM, SAT and VAT glucose uptakes were included. Plasmatic pro-inflammatory cytokine and adipokine levels were measured. Results: High VAT mean standardized uptake value (SUV) at baseline was associated with shorter eventfree survival (EFS) (hazard ratio [HR]: 7.89; 95% confidence interval [CI], 1.58-39.30; P = 0.012) and overall survival (OS) (HR, 15.24; 95% CI, 2.69-86.30; P = 0.002) among patients with newly diagnosed MM, even after adjustment for covariates. The highest tertile of VAT SUV was significantly correlated with worse MM-EFS (HR for the highest vs the lowest tertile 3.71; 95% CI, 1.22-10.56; Ptrend = 0.035) and mortality (HR, 4.41; 95% CI, 1.28-12.77; Ptrend = 0.019).

Notably, patients with higher VAT SUV presented with lower VAT area, VAT index, higher SAT SUV, and higher number of individuals with visceral obesity (all P < 0.01). Additionally, we found a negative correlation between VAT mean SUV with leptin (R2 = 0.20, P = 0.003); no correlations were detected between VAT mean SUV and resistin, tumor necrosis factor (TNF) or interleukin (IL)-6. Conclusions: Functional VAT activity estimated by 18F-FDG PET-CT is a relevant prognostic factor in MM patients, specifically, a higher VAT SUV might be an early biomarker of cancer cachexia in these patients. 0 2021 Elsevier Ltd and European Society for Clinical Nutrition and Metabolism. All rights reserved.

CLINICAL NUTRITION 40[6], 4075-4084, 252002 DOI 10.1016/j.clnu.2021.02.010

[P199-2021] "Vortex rings from high energy central p plus A collisions"

Lisa, M. A.; Barbon, J. G. P.*; Chinellato, D. D.*; Serenone, W. M.*; Shen, C.; Takahashi, J.*; Torrieri, G.*

Relativistic p + A collisions may produce droplets of quark-gluon plasma (QGP) that quickly develop a toroidal vortex structure similar to that of an expanding smoke ring. We present viscous relativistic hydrodynamic calculations of ultracentral p + A collisions and develop an experimental observable to probe the structure, correlating the polarization and momentum of hyperons emitted from the collision. This effect is robust against changes in the definition of vorticity used to calculate the polarization. Experiments at the Brookhaven National Laboratory Relativistic Heavy Ion Collider and the CERN Large Hadron Collider may test the existence and strength of the vortex toroids, bringing new evidence to bear on the question of collectivity in the smallest QGP droplets.

PHYSICAL REVIEW C 104[1], L011901, 2021. DOI 10.1103/ PhysRevC.104.L011901

Materiais Editoriais

[Ma002-2021] "Reply to "Comment on 'Unconventional enhancement of ferromagnetic interactions in Cd-doped GdFe2Zn20 single crystals studied by ESR and Fe-57 Mossbauer spectroscopies'"

Cabrera-Baez, M.; Munevar, J.; Couto-Mota, R. M.; Camejo, Y. M.; Contreras, C.; Baggio-Saitovitch, E.; Avila, M. A.; **Rettori,** C.*

The RT2Zn20 family offers an incredible versatility to tune diverse ground states through small modifications of their composition. In our recent publication [Phys. Rev. B 102, 144420 (2020)] we have reported an enhancement of the FM transition temperature due to negative chemical pressure from 86 to 96 K for x = 0.0 and x = 1.4, respectively, with an also unexpected, however, suspicious reduction of the effective and saturation magnetic moment that was inconsistent with our ESR data [Phys. Rev. B 102, 144420 (2020)]. In a comment of our work by Canfield (preceding paper [Phys. Rev. B 103, 176401 (2021)]), they have confirmed our finding about the enhancement of the FM temperature, however, with appreciable differences in the M(H) and M(T) curves for the Cd doped samples. We agree with their analysis of the magnetization data, the saturation of those samples is between 6 mu(B) and 7 mu(B) instead of 4 mu(B) as we have reported. It is indeed likely that we have used a mass value of the measured samples that includes Cd-doped GdFe2Zn20 and a second-phase contamination of the non-magnetic Zn flux (please observe the XRD data in the original paper [Phys. Rev. B 102, 144420 (2020)]). Therefore, we agree with the comment by Canfield et al.

(preceding paper [Phys. Rev. B 103, 176401 (2021)]) about the thorough analysis of the M(T) and M(H) for the Cd-doped samples (Fig. 2 of their Comment). The erratum clarifies and corrects Phys. Rev. B 103, 179903(E) (2021)].

PHYSICAL REVIEW B 103[17], 176402, 2021. DOI: 10.1103/ PhysRevB.103.176402

[Ma003-2021] "Simultaneous Imaging of Lung Perfusion and Glucose Metabolism in COVID-19 Pneumonia"

Ramos, C. D.; Fernandes, A. P.; Souza, S. P. M.; Fujiwara, M.; Tobar, N.; Dertkigil, S. S. J.; **Takahashi, M. E. S.***; Goncales, E. S. L.; Trabasso, P.; Zantut-Wittmann, D. E.

AMERICAN JOURNAL OF RESPIRATORY AND CRITICAL CARE MEDICINE 203[9], 1186-1187, 252002, 2021. DOI 10.1164/rccm.202007-2944IM

*Autores da comunidade IFGW Fonte: Web of Science on-line (WOS)

Patentes

[Pa001-2021] "DISPOSITIVO TERMOMAGNÉTICO RECIPROCATIVO LINEAR E USO DO MESMO"

Sergio Gama; Adelino de Aguiar Coelho; Isaias da Silva Número da Patente ou Registro: Agência INOVA BR102012012822-

Tipo: Patente de Invenção

Mês/Ano de Conclusão: 03/2021 - INPI/BRASIL

[Pa002-2021] "NANOPARTÍCULAS COM PROPRIEDADES ÓPTI-CAS DE FLUORESCÊNCIA E USO"

Marcelo Giannini; Rafael Rocha Pacheco; Frederick Allen Rueggeberg; Jorge Rodrigo Soto Montero; Eduardo David Martinez; Ali Francisco Garcia Flores; Ailla Carla Rocha Acosta Lancellotti; Guilherme Gorgen Lesseux; Carlos Rettori; Ricardo Rodrigues Urbano

Número da Patente ou Registro: Agência INOVA US20190183742

Tipo: Patente de Invenção

Mês/Ano de Conclusão: 05/2021 - INPI/BRASIL

[Pa003-2021] "SENSOR DIRECIONAL DE CURVATURA BASEA-DO EM FIBRAS ÓPTICAS ANTIRRESSONANTES"

Cristiano Monteiro de Barros Cordeiro; Marcos Antonio Ruggieri Franco

Número da Patente ou Registro: Agência INOVA BR 10 2021 006468 4

Tipo: Patente de Invenção

Mês/Ano de Conclusão: 04/2021 - INPI/BRASIL

[Pa004-2021] "Sistema híbrido de aquecimento de água e geração fotovoltaica com melhor aproveitamento da energia solar"

Newton Cesario Frateschi; Arthur Vieira da Silva Oliveira Número da Patente ou Registro: Agência INOVA PI1004669-0

Tipo: Patente de Invenção

Mês/Ano de Conclusão: 03/2021 - INPI/BRASIL

[Pa005-2021] "Sistema modular para elementos de fachada dinâmicos, método de operação do sistema e uso do mesmo"

Ana Lucia Nogueira de Camargo Harris; Denise Sayuri Sakaragui; Gabriella Bergamini; Bruno Eduardo Medina; Andre Luis Pissolatti

Número da Patente ou Registro: Agência INOVA BR102013023106-1

Tipo: Patente de Invenção

Mês/Ano de Conclusão: 01/2021 - INPI/BRASIL

Fonte: Sistema de Informação de Pesquisa e Extensão da Uni-

camp - SIPEX

Defesas de Dissertações do IFGW

[D012-2021] "Análise bayesiana de perfis laterais e longitudinais de chuveiros atmosféricos extensos"

Aluno: Pedro Rossini Sardelich

Orientador: Prof. Dr. José Augusto Chinellato

Data: 15/07/2021

[D013-2021] "Estudo da adsorção, conformação e reatividade de porfirinas brominadas em Cu(111)"

Aluno: Alisson Ceccatto dos Santos Orientador: Prof. Dr. Abner de Siervo

Data: 26/08/2021

[D014-2021] "Classicalidade e codificação superdensa no cenário de preparação e medição"

Aluno: Carlos Augusto Belini de Gois

Orientador: Prof. Dr. Rafael Luiz da Silva Rabelo

Data: 27/08/2021

[D015-2021] "Investigação da viabilidade do uso de conectividade funcional baseada em EEG para caracterização da atividade interictal na epilepsia do lobo temporal mesial"

Aluno: Leonardo Rodrigues da Costa Orientador: Profa. Dra. Gabriela Castellano

Data: 27/08/2021

Defesas de Teses do IFGW

[T008-2021] "Optomecânica integrada: experimentos clássicos e quânticos em osciladores massivos"

Aluno: Rodrigo da Siva Benevides

Orientador: Prof. Dr. Thiago Pedro Mayer Alegre

Data: 16/06/2021

[T009-2021] "Termodinâmica a tempo finito em atalhos para adiabaticidade e máquinas de Szilárd"

Aluno: Thiago Vaz Acconcia

Orientador: Prof. Dr. Marcus Vinicius Segantini Bonanca

Data: 12/07/2021

[T010-2021] "Aspectos termodinâmicos em teoria da res-

posta linear"

Aluno: Pierre Marie Antoine Leite Nazé

Orientador: Prof. Dr. Marcus Vinicius Segantini Bonança

Data: 29/07/2021

[T011-2021] "Propriedades mecânicas do gelo Ih e propriedades estruturais e dinâmicas da água super-resfriada"

Aluno: Ingrid de Almeida Ribeiro

Orientador: Prof. Dr. Maurice de Koning

Data: 13/08/2021

Fonte: Portal IFGW/Pós-graduação - Agenda de Colóquios,

Defesas e Seminários.

Disponível em: http://portal.ifi.unicamp.br/pos-graduacao

Defesas de Teses e Dissertações do PFCIM

Observação: Não ocorreram neste período defesas de teses e dissertações, com orientadores ou banca do IFGW, do Programa de Pós-Graduação Multiunidades em Ensino de Ciências e Matemática - Mestrado e Doutorado (PECIM) da Unicamp.

Fonte: Página do PECIM

Disponível em: https://www.pecim.unicamp.br/bancas

Abstracta

Instituto de Física "Gleb Wataghin" - IFGW Diretora: Profa. Dra. Mônica Alonso Cotta Diretor Associado: Prof. Dr. Marcos Cesar de Olivei-

ra

Universidade Estadual de Campinas - UNICAMP

Cidade Universitária Zeferino Vaz 13083-859 - Campinas - SP - Brasil e-mail: secdir@ifi.unicamp.br

Fone: +55 19 3521-5300

Publicação

Biblioteca do Instituto de Física Gleb Wataghin http://portal.ifi.unicamp.br/biblioteca

Diretora Técnica: Sandra Maria Carlos Cartaxo Coordenadora da Comissão de Biblioteca: Profa. Dra. Arlene Cristina Aguilar

Elaboração:

Maria Graciele Trevisan (Bibliotecária)

Ayres Neri da Cunha Junior (Técnico Administrativo)

contato: infobif@ifi.unicamp.br